Clustering wind profile shapes to estimate airborne wind energy production

Mark Schelbergen[1], Peter C. Kalverla[2], Roland Schmehl[1], and Simon J. Watson[1]

[1]Faculty of Aerospace Engineering, Delft University of Technology, Kluyverweg 1, 2629 HS Delft, The Netherlands
[2]Meteorology and Air Quality Section, Wageningen University, PO box 47, 6700 AA Wageningen, The Netherlands

Correspondence: Mark Schelbergen (m.schelbergen@tudelft.nl)

Abstract. Airborne wind energy (AWE) systems harness energy at heights beyond the reach of tower-based wind turbines. To estimate the annual energy production (AEP), measured or modelled wind speed statistics close to the ground are commonly extrapolated to higher altitudes, introducing substantial uncertainties. This study proposes a clustering procedure for obtaining wind statistics for an extended height range from modelled datasets that include the vertical variation of the wind speed and direction. K-means clustering is used to identify a set of wind profile shapes that characterise the wind resource. The methodology is demonstrated using the Dutch Offshore Wind Atlas for the locations of the met masts IJmuiden and Cabauw, 85 km off the Dutch coast in the North Sea and in the centre of the Netherlands, respectively. The cluster-mean wind profile shapes and the corresponding temporal cycles, wind properties, and atmospheric stability are in good agreement with literature. Finally, it is demonstrated how a set of wind profile shapes and their statistics are used to estimate the AEP of a small-scale pumping AWE system located at Cabauw, which require the derivation of a separate power curve for each shape. Studying the relationship between the calculated AEP and the number of site specific clusters used for the calculation shows that the AEP error is within three percent of the converged value for four or more clusters.

1 Introduction

Airborne wind energy (AWE) systems use tethered flying devices to harness energy at higher altitudes than tower-based wind turbines, typically heights above 150 m (Malz et al., 2019; Salma et al., 2019), where wind is generally stronger and more persistent. For estimating annual energy production (AEP), wind speed statistics in the full operational height range of the AWE system are commonly approximated by extrapolating the wind speed distribution close to the ground to higher altitudes using either the wind profile power law or the logarithmic profile (e.g., Heilmann and Houle, 2013). This way of representing the wind resource introduces substantial uncertainties since the aforementioned wind profile relationships are not strictly valid beyond the surface layer. Moreover, within this layer, not all wind profiles can be described well with these relationships.

The power law is a simple empirical relationship which can be used to relate the wind speed u at one height z_1 to that at a different height z_2 and has the form:

$$u(z_2) = u(z_1)\left(\frac{z_2}{z_1}\right)^{\alpha} \quad , \tag{1}$$

where α is an empirical shear exponent factor related to the surface properties. The power law is normally applied up to around 100–$200\,\mathrm{m}$ (Peterson and Hennessey, 1978), and does not offer enough flexibility to describe the variety of measured wind profiles (e.g., Park et al., 2014).

The logarithmic wind profile is frequently used to estimate the variation in wind speed with height over a flat surface. This profile is based on physical arguments and a form of the profile has been well established based on Monin-Obukhov similarity theory (Monin and Obukhov, 1954). In this non-adiabatic form, the mean wind speed u at height z is given by:

$$u(z) = \frac{u_*}{\kappa}\left[\ln\left(\frac{z}{z_0}\right) - \Psi\left(\frac{z}{L}\right)\right] \quad, \tag{2}$$

in which u_* is the friction velocity, κ is the von Karman constant, z_0 is the roughness length, Ψ is a stability correction function, and L is the Obukhov length that is often used to evaluate atmospheric stability and is positive (negative) for stable (unstable) stratification and infinite for neutral stratification. Holtslag et al. (2014) proposes the following stability correction functions:

$$\Psi\left(L \leq 0\right) = 2\ln\left(\frac{1+x}{2}\right) + \ln\left(\frac{1+x^2}{2}\right) - 2\arctan\left(x\right) + \frac{\pi}{2}, \qquad x = \left(1 - 19.3\frac{z}{L}\right)^{\frac{1}{4}} \quad, \tag{3}$$

$$\Psi\left(L \geq 0\right) = -6.0\frac{z}{L} \quad. \tag{4}$$

Although the assumptions underlying the logarithmic wind profile are frequently violated in practice (e.g., Optis et al., 2014), it is widely used, particularly for wind resource estimation.

The value of L is not easily measured or derived from model data and is generally inferred indirectly. One way to do this is to fit a functional form of the logarithmic wind profile with stability correction to the wind velocity magnitude profile. Such an approach is outlined by Basu (2018), using three levels of wind speed. Another common way of estimating L, is by inferring it from the gradient Richardson number, $\mathrm{Ri_G}$. We approximate this number using a finite difference, yielding the bulk Richardson number, $\mathrm{Ri_B}$, which expresses the ratio between the temperature stratification and the wind shear:

$$\mathrm{Ri_B} = \frac{\frac{g}{\bar{\theta}_\nu}\Delta\theta_\nu\Delta z}{\Delta u^2 + \Delta v^2} \quad, \tag{5}$$

in which g is the gravitational acceleration, $\bar{\theta}_\nu$ is the mean virtual potential temperature, and $\Delta\theta_\nu$, Δu, and Δv are the virtual potential temperature and the two horizontal wind component differences, respectively, determined over the height difference Δz. Positive (negative) $\mathrm{Ri_B}$ values indicate stable (unstable) stratification and values close to zero indicate neutral stratification. By assuming a functional form of the stability correction, L can be derived from $\mathrm{Ri_B}$ (Holtslag et al., 2014):

$$\frac{z}{L} = \begin{cases} \frac{\mathrm{Ri_B}}{1-5\mathrm{Ri_B}}, & \text{if } \mathrm{Ri_B} \geq 0 \\ \mathrm{Ri_B}, & \text{otherwise} \end{cases} \quad, \tag{6}$$

in which z is a reference height which is commonly taken as either the arithmetic or geometric mean of the heights used to determine the temperature and wind speed differences.

The wind direction can vary substantially with height, also in the lower atmosphere (e.g., Brown et al., 2005; Floors et al., 2015). As they are scalar quantities, both the power law and logarithmic profile wind speed relationships provide no information about any wind direction dependence with height. In addition, the relationships assume that wind speed increases monotonically with height. In practice, low-level maxima in wind speed, with decreasing wind speed above (low-level jets), are likely to occur, which is also observed in reanalysis data (e.g., Ranjha et al., 2013; Kalverla et al., 2019). To extend the validity of wind profile relationships to higher altitudes, several modifications have been proposed (e.g., Gryning et al., 2007; Holtslag et al., 2017). However, these theoretical formulations are only validated up to heights relevant for conventional, tower-based wind turbines.

Alternatively, computationally expensive, brute-force energy production calculations do not assume any wind profile relationship and are performed using historical wind data for the full operational height range. Bechtle et al. (2019) use ERA5 reanalysis data to map out the wind resource available to AWE systems over a large part of Europe, but do not touch upon the respective power production of an AWE system. Ranneberg et al. (2018) combine COSMO-DE reanalysis data with power curves for multiple heights, that are independent of the wind profile shape, to estimate the AEP. This is a valid approach if the system is operating at a nearly constant height. However, the wind profile shape has to be considered if the system operates in a larger height range, as is the case for a flexible-kite AWE system (Van der Vlugt et al., 2019). AEP calculations become more computationally expensive if the wind profile is considered, especially when optimising the cycle settings for all time points. Malz et al. (2020a) use three months of three-hourly MERRA-2 reanalysis data and speed up the computation by a factor 20 by using the solution of the previous optimisation to initialise the next. In a follow-up study, Malz et al. (2020b) use this approach to determine the AEP of an AWE system for 16 locations in Europe. The current state-of-the-art is lacking a methodology that can be confidently used to make efficient AEP calculations for a pumping AWE system that sweeps a non-negligible height range.

Previously, clustering techniques have been used for identifying wind profile patterns. Sommerfeld et al. (2019) applies k-means clustering to subdivide stable and unstable wind profile datasets from lidar observations into two clusters for a location in a mostly flat area in northern Germany. Duran et al. (2019) use self-organising maps to characterise wind profile data for two locations (Cabauw in the centre of the Netherlands and the FINO-1 platform in the North Sea, 45 km north of the German/Dutch coast) from Weather Research and Forecasting modelled data using 2300 clusters. The clusters are used for forecast verification and to investigate diurnal and seasonal cycles.

This study proposes a clustering procedure for obtaining wind profiles from modelled data that includes the vertical variation of the wind speed and direction. The data are partitioned into a small number of clusters and the corresponding cluster-mean wind profile shapes are determined. We have chosen an empirical approach for identifying these shapes such that they are not restricted by physical assumptions. Nevertheless, we try to physically interpret the observed features. In contrast to earlier studies that use clustering, we investigate normalised wind profiles, as these are often described by wind profile relationships and yield a more compact wind resource representation. Moreover, the variation of the wind direction with height is included as it affects the operation of an AWE system.

The following sections of this paper outline the process of making an efficient AEP estimation for an AWE system based on historical wind data. Section 2 introduces the Dutch Offshore Wind Atlas (DOWA) and ERA5 datasets. Section 3 discusses the

data processing and clustering techniques, complemented by interim results. Section 4 first addresses the clustering of DOWA data, for which the results are presented for an on- and offshore location. Subsequently, the DOWA data of 45 other locations is clustered altogether to generate a generalised set of wind profile shapes that is applicable for an area which includes a wide range of location types. Although the resulting wind resource representation can be used for other applications, we illustrate its use for estimating the AEP of pumping AWE systems. Section 5 demonstrates the AEP estimation for a flexible-kite AWE system and assesses how many wind profile shapes (clusters) are required for an accurate estimation. Finally, Sect. 6 summarises the conclusions of this study.

2 Wind datasets

In principle, datasets containing time series of wind speeds and directions for multiple altitudes can be used as input for the proposed methodology. For the AEP calculation, we focus on the sensitivity of the power production of an AWE system to the wind profile, which is assumed to be steady-state in the calculation. An hourly temporal resolution of the datasets suffices for capturing the diurnal cycle of the wind profile. While smaller scale atmospheric phenomena might have an (adverse) effect on the power production, these effects are typically superimposed on a steady-state wind profile using separate models for assessing, e.g., the associated loss in power production (Fechner, 2016). This power loss is device-specific and depends on control strategy, and is therefore not considered here. The first commercial AWE initiatives envisage a maximum operational height of $500\,\text{m}$ because operation at higher altitudes requires more complex system designs (Watson et al., 2019, p. 4) and legislative procedures (Salma et al., 2018). For the wind resource representation for AWE, it is thus desirable to have wind data at least up to this height. The vertical resolution should be adequate to assess the shape of the wind profile with sufficient detail for the performance calculations. Both long-term lidar observations and modelled data qualify as input. This study focuses on using modelled data, which provides good spatial and temporal coverage.

A typical on- and offshore location in the Netherlands and the North Sea, respectively, are selected for demonstrating the methodology. The offshore location, that of the met mast IJmuiden, is located $85\,\text{km}$ off the Dutch coast in the North Sea. The onshore location, namely, the met mast Cabauw, is located in the centre of the Netherlands. The area surrounding the mast is flat open grass-land for at least $400\,\text{m}$ in all directions and up to $2\,\text{km}$ in the dominant wind direction, i.e. west-south-west. Within a radius of $20\,\text{km}$, the terrain is predominantly grass-land and is virtually flat. Note that no anemometer or lidar measurements are analysed. We only analyse down-scaled reanalysis data for these sites. The sites were chosen as they are well-known in the literature. Figure 1 shows where in the Netherlands they are situated. The other 45 depicted locations are used to evaluate the full DOWA domain and are selected such that onshore, coastal, and offshore locations are equally represented. The datasets for the met masts Cabauw and IJmuiden and the 45 locations are referred to as the onshore, offshore, and multi-location datasets, respectively.
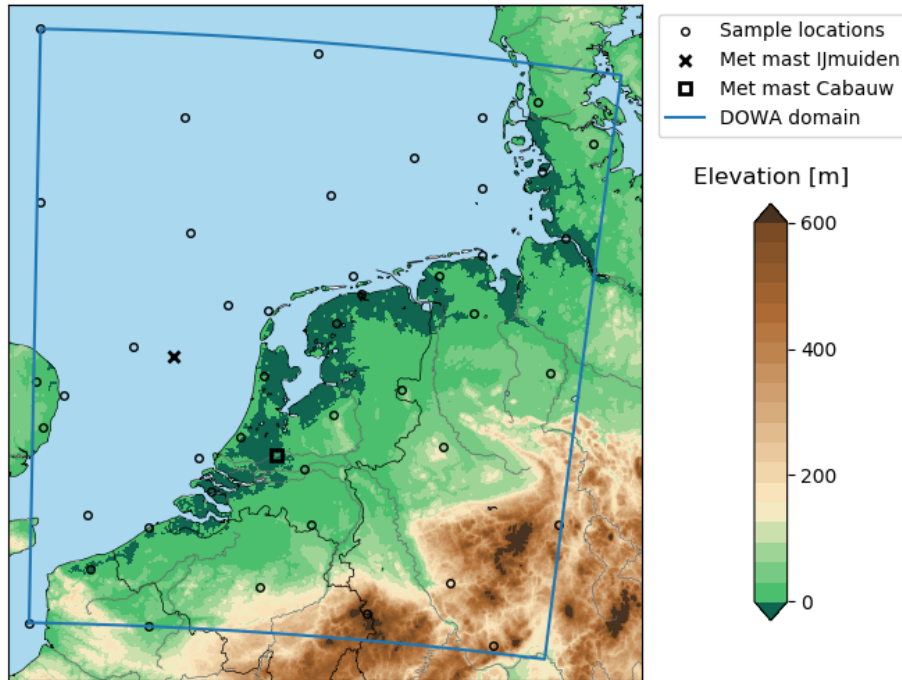
Figure 1. The DOWA domain, framed by the blue line, covers the Netherlands, a substantial part of the North Sea, and adjoining coastal areas. The ×, □, and ○ markers depict the locations analysed in Sect. 4.1, 4.3, and 4.4, respectively. The sea is depicted in light blue and the colour scale shows the elevation of the land surface (Amante and Eakins, 2009).

2.1 ERA5

ERA5 (Copernicus Climate Change Service, 2017) is a global reanalysis produced by ECMWF using their integrated forecasting system, namely ECMWF's atmospheric model and data assimilation system. At the time of writing, ERA5 data is available from 1979 to the present time. The data includes hourly modelled values of a large number of atmospheric variables on a 30 km
5   horizontal grid with 137 vertical pressure levels up to a height of roughly 80 km. The level heights are time dependent and interpolation is needed to obtain the wind data for fixed heights as required by the presented methodology. The clustering of the wind profiles is performed using the DOWA data, which is described in the following section. As explained later on, ERA5 is only used to determine the atmospheric stability at the time and location of the analysed wind profiles.

2.2 Dutch Offshore Wind Atlas

10   The DOWA (Wijnant et al., 2019) is based on the ERA5 reanalysis and downscaled to a finer-resolution surface grid using the mesoscale weather model HARMONIE-AROME (Bengtsson et al., 2017). The downscaled reanalysis is performed for 10 years from 2008 until 2017. Hourly values for temperature, wind speed and direction, pressure and relative humidity are made available on 2.5 km grid (217 x 234 points) and 17 heights between 10 and 600 m. The DOWA domain is illustrated in

Fig. 1. Due to the higher resolution and non-hydrostatic nature of HARMONIE-AROME, DOWA benefits from an improved representation of the coastline, land surface heterogeneity, and mesoscale circulations, such as the sea breeze. Furthermore, additional observations from routine weather stations, satellite retrievals (ASCAT), and aircraft sensors (MODE-S EHS) have been assimilated by the HARMONIE-AROME model. Kalverla (2019) shows that DOWA improves on ERA5 in terms of wind speed, wind shear, and directional accuracy, as well as the representation of anomalous events such as low-level jets.

3 Clustering procedure

This section illustrates the clustering procedure for the offshore location. The data is filtered and normalised and its dimensions are reduced using a principal component (PC) analysis. Next, the clustering performance is analysed and the number of clusters is chosen for the wind resource representations analysed in Sec. 4.

3.1 Preprocessing of the wind data

The operation of an AWE system is affected by the variation of the wind speed and direction with height. Therefore, the wind profile shapes are studied with both these features included. Each wind profile sample consists of wind velocities for multiple heights (vertical grid points) at a given time and location and is processed using its own properties in two steps to obtain its shape. The wind velocities are originally expressed by their easterly and northerly wind speed components. Firstly, similar to Kalverla et al. (2017) and Malz et al. (2020a), the wind speed components are expressed as components parallel and perpendicular to the reference wind velocity at $100\,\mathrm{m}$ for every sample, which makes the wind profiles independent of their reference wind directions. As a result, the perpendicular wind speed profiles are zero at $100\,\mathrm{m}$. Secondly, the 90th percentile of the sample's wind velocity magnitudes is used to normalise the wind speed components. The normalised parallel and perpendicular wind speeds of a sample is referred to as the wind profile *shape* throughout this paper. Fewer outlying wind profile shapes result when the 90th percentile instead of, e.g., the maximum value is taken as normalisation value. The normalisation yields a more compact wind resource representation. However, it is prone to producing eccentric wind profile shapes for low winds. Therefore, the wind profiles that have a mean wind speed below $5\,\mathrm{m\,s^{-1}}$ are filtered out before clustering. Note that the low wind conditions have a small contribution to the AEP of a wind energy system and their wind profile shapes are thus of small importance for the AEP calculation. Although the results presented in Sects. 3 and 4 do not account for the the low wind samples, the wind resource representation for the AEP calculation in Sect. 5 does.

3.2 Principal component analysis of the wind profile shape dataset

Prior to clustering, a PC analysis is used to reduce the dimensionality of the dataset, while preserving most of the variance. This reduces the computational effort and thus speeds up the clustering. The PC analysis specifies a transformation from the original to the PC coordinate system with its origin at the mean of the dataset. The first axis is oriented such that it accounts for most of the variance in the data. Subsequent axes are perpendicular to their predecessors and oriented such that they account

for as much of the variance as possible. As a result, the last axis accounts for least of the variance. The PCs are unit vectors in the direction of the positive PC axes.

The mean wind profile shape for the offshore location is shown in the upper left panel of Fig. 2. As expected for an offshore location, the mean shape exhibits low wind shear. Moreover, in accordance with Ekman theory, the mean shape shows wind veer (wind direction turns clockwise with height), which can be observed in the hodograph (top-view) in the lower left panel of Fig. 2. A logarithmic profile with roughness length z_0=0.0002 m, a representative value for open water (Wijnant et al., 2015), is fitted to the lowest 200 m of the mean shape. We use this layer as a proxy for the 'surface layer', though in very stable situations the surface layer could be considerably smaller. Consequently, we consider applying the logarithmic profile relationship up to 200 m valid. Following the approach recommended by Kelly and Gryning (2010), the profile is fitted by varying the friction velocity u_* and the stability function Ψ, which we constrain to the functional forms given in Eqs. 3 and 4. From this, a mean value of the Obukhov length L can be inferred. The best fit profile corresponds to a value L=-3391 m, implying a neutral logarithmic profile in the surface layer (assuming neutral conditions if $|L| > 500$). Above 200 m, the fit slightly deviates from the mean profile.

The first two PC unit vectors are shown in the second column of Fig. 2, which illustrates how much each normalised wind speed component contributes to the unit vectors. The contributions of the perpendicular wind speed components account for most of PC1, indicating that PC1 characterises mostly wind veer. In contrast, the contributions of the parallel wind speed components account for most of PC2, indicating that PC2 characterises mostly wind shear. Both PCs show large contributions at both ends of the height range, which indicates that most variance in the dataset is found at these heights. The features of the dataset are no longer (normalised) physical properties, but contain contributions of all the normalised wind speed components. The third and fourth columns of Fig. 2 illustrate how the wind profile shapes vary with respect to the mean along PC1 and PC2. The wind veer differs substantially between wind profile shape 1 and 2 and the wind shear between 3 and 4.

The percentage of variance retained after dimensionality reduction depends on how many PCs are used to express the data and is calculated by the sum of the eigenvalues of the retained PCs divided by the sum of the eigenvalues of all components. Figure 3 shows that the first four PCs already account for more than 90 % of the variance in the offshore dataset. Since the wind velocities of neighbouring vertical grid points are highly correlated, most of the variance in the data is retained using a limited number of PCs. We consider retaining 90 % or more acceptable for our application. Since the variance retained still increases a few percent between four and five PCs, we opt for using five PCs. The preprocessed data is mapped onto the PC1–5-space and used as input for the clustering.

Figure 4a shows the frequency distribution of the wind profile shapes in the PC1, PC2-space. The PC1, PC2-projection of the wind profile shapes in the third and fourth columns of Fig. 2 are indicated with the markers. By visual inspection, two relatively dense groups of data points are identified: a confined group and a less confined group which resembles a tail extending from the first group, marked with the left and right ellipses, respectively. Figure 4b will be discussed in Sect. 4.3.
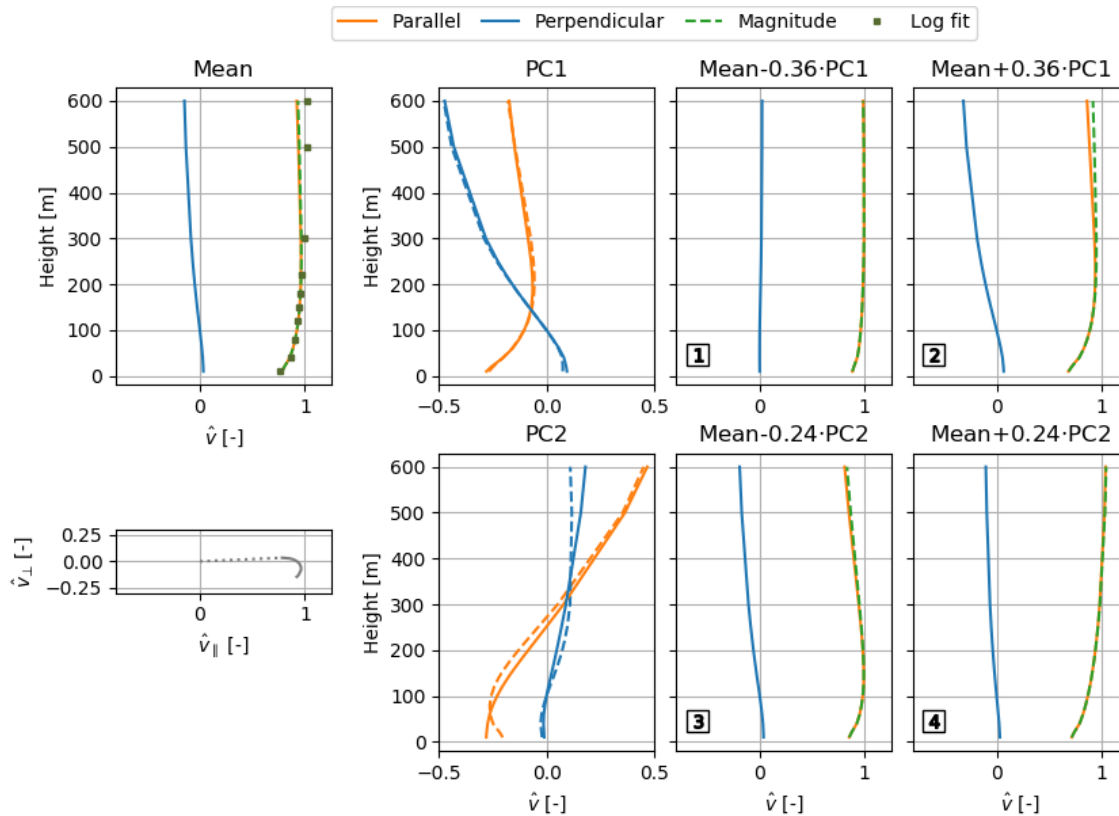
Figure 2. Mean wind profile shape and corresponding logarithmic profile fit (top-left) and corresponding hodograph (bottom-left), composition of the first and second PCs (second column), and PC multiplicands superimposed on the mean wind profile shape (using minus and plus one standard deviation as multipliers for the third and fourth columns, respectively) for the filtered offshore dataset. The wind profile shape numbers 1–4 refer to the markers in Fig. 4a. The average PC profiles of the two reference locations are plotted alongside the offshore PCs using the dashed lines (second column).

3.3 Choosing the number of clusters

K-means clustering (Pedregosa et al., 2011) is employed to identify the set of wind profile shapes that are used for representing the wind resource. Each cluster is represented by a centroid and each sample is assigned to the cluster with the nearest centroid. The clustering algorithm iteratively searches for the positions of the centroids that minimise the sum of the (squared) Euclidean distances between the centroids and their associated samples. This cost function is also referred to as the within-cluster sum of squares (WCSS). The resulting centroids reflect the *cluster-mean wind profile shapes* in the dataset, which follow from back-transforming the cluster-centroids from the PC to physical space.

K-means clustering is always able to produce a result, which makes it very powerful but also potentially deceptive. The algorithm tends to produce spherical clusters with equal radius and sample size, and works best on data with such a structure.
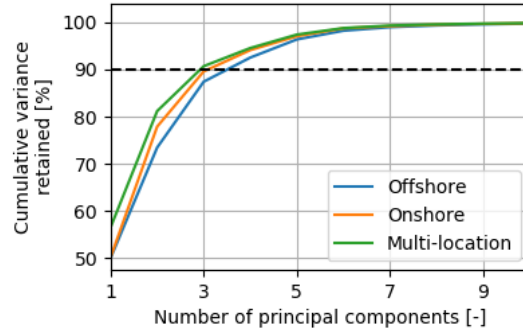
Figure 3. Relationship between the percentage of variance retained and the number of PCs for the filtered offshore, onshore, and multi-location datasets analysed in Sect. 4.1, 4.3, and 4.4, respectively.

(a) Offshore location   (b) Onshore location
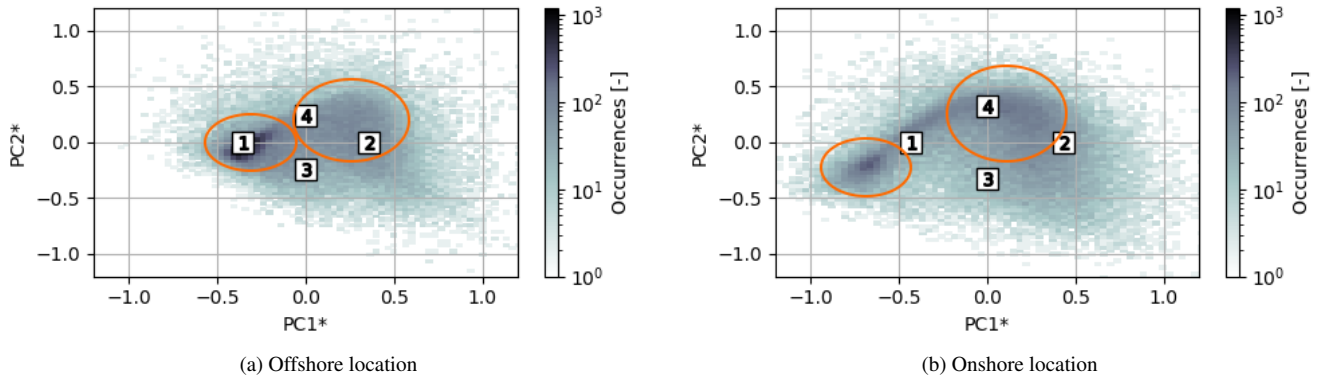
Figure 4. Sample frequency distributions in the PC1, PC2-space. The origins coincide with the mean wind profile shapes and the wind profile shapes numbered 1–4 in Figs. 2 and 11 are situated exactly one standard deviation away from the means. The orange ellipses indicate the visually identified clusters. The coordinate system represents the average PC profiles of the two reference locations, denoted by an asterisk and shown in Figs. 2 and 11.

Moreover, the result is highly sensitive to the choice of the number of clusters k and it is often not evident how many clusters to choose. The elbow and silhouette method are used for finding an appropriate number for k. Moreover, the choice for k is evaluated in the context of employing the cluster-mean wind profile shapes to represent the wind resource.

The elbow method investigates the trend of WCSS against k. Increasing the number of clusters is equivalent to reducing the WCSS. Kinks in the trend indicate appropriate choices for k. The elbow plot in the upper left panel of Fig. 5a shows no distinct kinks for more than three clusters.

The silhouette score expresses the similarity of a sample to the other samples in its cluster with respect to its similarity to the nearest neighbouring cluster's samples. The dimensionless score ranges from -1 to 1: a negative value suggests that the sample is assigned to the wrong cluster, a value around zero indicates that the sample lies between two clusters, and a high value indicates that the sample is assigned to a distinct cluster. The middle left panel of Fig. 5a shows the mean silhouette
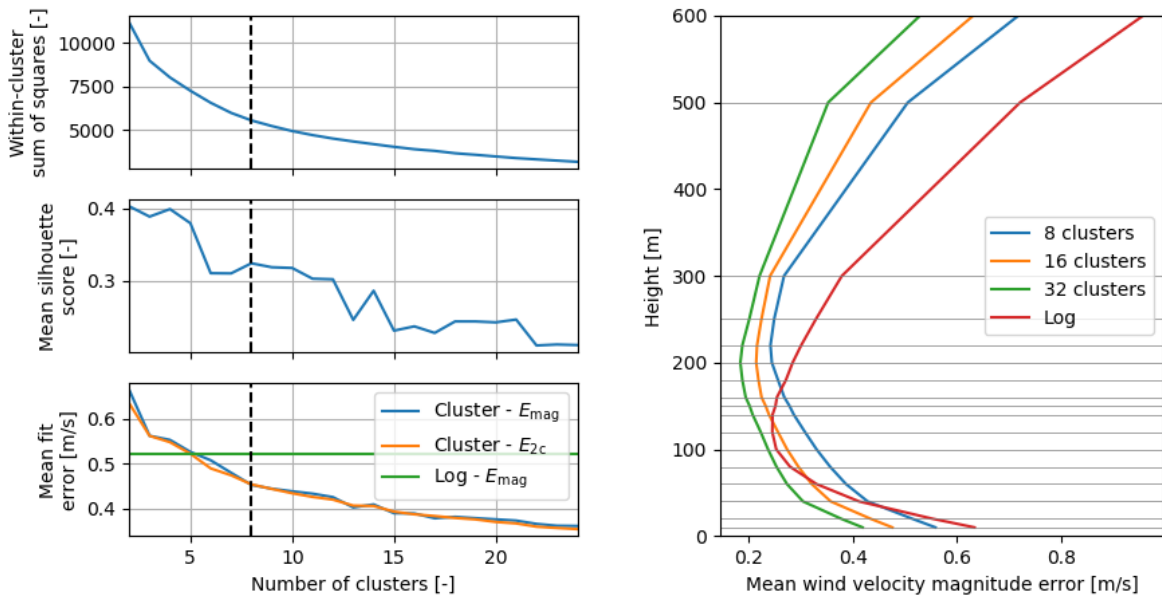
(a) The cost function of the clustering algorithm (top), the cluster cohesiveness metric (middle), and the mean wind speed fit error (bottom) against the number of clusters. The dashed vertical lines depict the final choice for eight clusters.

(b) Mean wind velocity magnitude error with height for the cluster and logarithmic representations.

Figure 5. Sensitivity of the clustering performance to the number of clusters over the full vertical grid (a) and for each height point (b) for the filtered offshore dataset.

score is highest for two clusters. The division of the dataset into two clusters thus yields the most cohesive clusters, which is in agreement with the visual inspection of Fig. 4a. The decreasing trend of silhouette score with k implies that, in general, a small number of clusters should be used to maintain cluster cohesiveness.

After obtaining the cluster-mean wind profile shapes, they are used for constructing the *cluster representation* of the wind resource. Each sample's vertical wind variation is approximated by de-normalising the cluster-mean wind profile shape of the cluster to which it is assigned using the normalisation wind speed of the pre-processing. We assess the accuracy of the cluster representation using the mean sample fit error. The fit error of an individual sample is assessed by the magnitude and two-component root mean square fit errors over all the 17 DOWA vertical grid points. The representation accuracy is evaluated by the mean of all filtered samples for the two sample fit error expressions, E_{mag} and $E_{2\mathrm{c}}$, respectively:

$$E_{\mathrm{mag}} = \frac{1}{n_{\mathrm{s}}} \sum_{j=1}^{n_{\mathrm{s}}} \left(\sqrt{\frac{1}{n_{\mathrm{h}}} \sum_{i=1}^{n_{\mathrm{h}}} \varepsilon_{i,j}^2} \right) \tag{7}$$

and

$$E_{2c} = \frac{1}{n_s} \sum_{j=1}^{n_s} \left(\sqrt{\frac{1}{2 n_h} \sum_{i=1}^{n_h} \left(\varepsilon_{\parallel,i,j}{}^2 + \varepsilon_{\perp,i,j}{}^2 \right)} \right) \quad , \tag{8}$$

in which n_h is the number of heights, n_s is the number of samples, $\varepsilon_{i,j}$ is the wind velocity magnitude error, and $\varepsilon_{\parallel,i,j}$ and $\varepsilon_{\perp,i,j}$ are the parallel and perpendicular wind speed errors, respectively, at each vertical grid point i for the jth sample.

5   Alternatively, logarithmic profiles can be used to approximate the vertical wind variations of the samples in a wind resource representation. This logarithmic representation is obtained by fitting logarithmic profiles with roughness length $z_0=0.0002\,\text{m}$ to every sample. Here, the value of the Ψ stability function is restricted to one of the values corresponding to the five stability classes, which follow from the Obukhov lengths L in the third column of Table 1. Moreover, the fit is performed to the full height range, i.e. 10–600 m, as we aim to minimise the fit error of the wind resource representation and, therefore, allow

10   applying the logarithmic profile relationship beyond the surface layer. As the logarithmic representation does not include information about the wind direction variation with height, it is only assessed using E_{mag}.

Table 1. Stability classes in terms of the Obukhov length, adapted from Holtslag et al. (2014).

Class name	Class boundaries [m]	Representative L [m]
Very unstable (VU)	$-200 \le L < 0$	-100
Unstable (U)	$-500 \le L < -200$	-350
Neutral (N)	$|L| > 500$	10^{10}
Stable (S)	$200 < L \le 500$	350
Very stable (VS)	$0 < L \le 200$	100

We consider the usage of the cluster representation valid when it yields a higher accuracy than the logarithmic representation. To this end, we evaluate the fit error of the cluster representation in relation to the number of clusters and compare it to the fit error of the logarithmic representation. Figure 5a shows that whether the error of the cluster representation is evaluated

15   using E_{mag} or E_{2c} makes little difference. Note that the WCSS scales quadratically with the mean fit error of the cluster representation. The cluster representation is more accurate than the logarithmic representation when using three clusters or more.

The fit error is also evaluated for all vertical grid points separately to evaluate their contributions to the mean fit error. The mean value of the wind velocity magnitude errors of all filtered samples ($\bar{\varepsilon}_i$) is shown for each vertical grid point in Fig. 5b.

20   The fits have a relatively low mean wind speed error around 150 m height and a higher error at the top and bottom. The horizontal lines depict the 17 heights of the DOWA vertical grid. Around 150 m height, the grid is relatively fine, which is equivalent to allocating more weight to the 100–200 m interval for the logarithmic profile fitting procedure. As a result, the fitting favours minimising the errors in this interval over those at both ends of the height range. Note that the sensitivity of the

cluster representation to the grid spacing is limited by the PC analysis prior to the fitting. As stated before, the PC1 and PC2 profiles show that most variance in the dataset is found at both ends of the height range. Due to the relatively high variance and fit model deficiencies, the fit error is also expected to be largest at these heights. Although the error of the cluster representations at 100 m is higher than that of the logarithmic representation, on average they perform substantially better.

5   The analysis in Sect. 4 requires a limited number of clusters to represent the wind resource. The choice for eight clusters follows from a trade-off between the mean wind profile fit error, the silhouette score, representation validity, and our aim to present a meaningful analysis and interpretation of the resulting clusters. To get more insight in the structures of the eight offshore clusters (MMIJ-1–8), the mean silhouette score is calculated for each cluster. The higher the mean silhouette score, the more likely that a cluster is representing a natural structure in the data. Figure 6 shows that a large fraction of the samples

10   have high silhouette scores for MMIJ-1–4, indicating that MMIJ-1–4 are relatively cohesive clusters. The silhouette score distributions of MMIJ-5–8 indicate less uniform sets of samples, especially that of MMIJ-8. Note that MMIJ-1 is roughly a factor 2.5 larger than the second biggest cluster despite the tendency of k-means clustering to produce equally sized clusters.
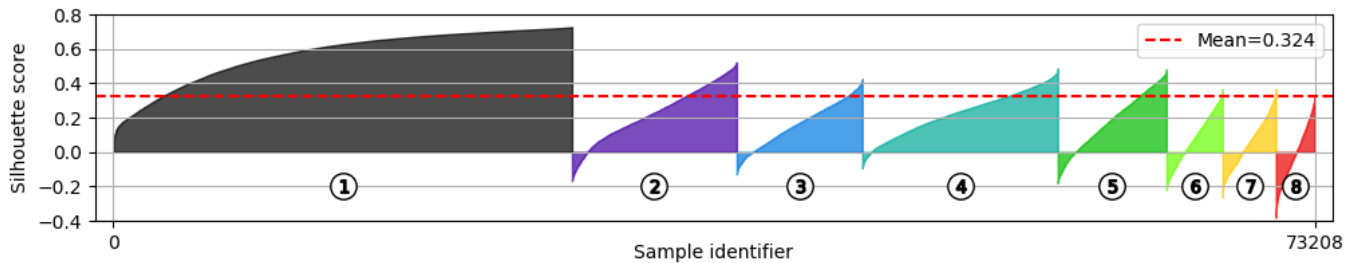
Cluster label	MMIJ-1	MMIJ-2	MMIJ-3	MMIJ-4	MMIJ-5	MMIJ-6	MMIJ-7	MMIJ-8	overall
Mean silhouette score	0.567	0.226	0.164	0.226	0.184	0.080	0.056	-0.009	0.324

Figure 6. The silhouette scores of the individual samples grouped by cluster and in ascending order for the filtered offshore dataset. The numbered markers and filled area colours indicate to which cluster the sample belongs. The overall mean score is indicated by the dashed line and the table below the figure states the mean score for each cluster.

| (a) Offshore location | (b) Onshore location |
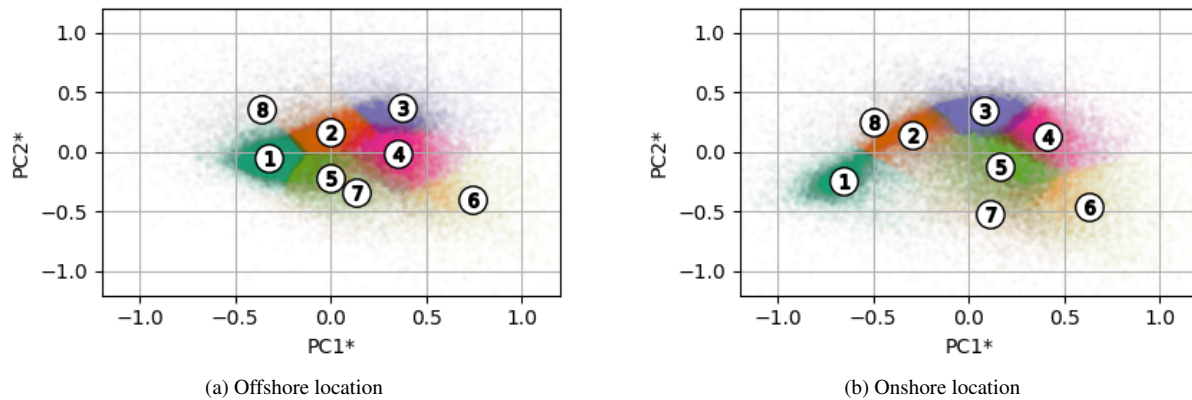
Figure 7. Projection of the samples onto the PC1, PC2-space. The colour indicates to which cluster a sample belongs and the markers represent the cluster-centroids. The coordinate system represents the average PC profiles of the two reference locations, denoted by an asterisk and shown in Figs. 2 and 11.

4   Cluster wind resource representation

This section discusses the physical interpretation of the cluster representations. Firstly, the clusters and their cluster-mean wind profile shapes that result from the offshore dataset are presented. For each cluster, patterns in the times of occurrences are studied together with their association to wind properties at 100 m and atmospheric stability. The analysis is then repeated for
5   the onshore location. Comparing the cluster sets for both reference locations sheds some light on the their general applicability. Finally, data from 45 locations are combined to obtain a single set of clusters that is applicable for the full DOWA domain. For each of the resulting clusters, a map is generated depicting the cluster frequency distribution over the DOWA domain.

4.1   Cluster representation for the offshore location

The clustering of the dataset for the offshore location of the met mast IJmuiden yields eight clusters (MMIJ-1–8), which are
10   represented by centroids shown in Figure 7a. The clusters are well spread over the PC1, PC2-space, with the exception of MMIJ-5 and 7, which are relatively close to each other. Note that only two axes of the five-dimensional PC-space are shown. Table 2 lists all five PC-coordinates of the cluster-centroids and confirms that the PC1 and PC2 coordinates of MMIJ-5,7 are similar, in contrast to their PC3 coordinates: the centroids are furthest apart along PC3. The PC4 and PC5 values have a substantially smaller range than that for PC1–3 and are superfluous for distinguishing between the eight clusters.
15   The cluster-mean wind profile shapes of the offshore clusters are shown in Fig. 8. Logarithmic profiles with roughness length z_0=0.0002 m are fitted to the magnitude profiles and shown for comparison. Here, the stability function is varied continuously and the fit is restricted to the lower 200 m. The values found for the corresponding Obukhov lengths are assigned to the stability classes in Table 1 and plotted as $500\,\mathrm{m}/L$ in Fig. 9. The comparison serves to show to what extent the cluster shapes deviate from non-adiabatic logarithmic profiles, particularly above the surface layer.

Table 2. Principal component coordinates of the cluster-centroids for the filtered offshore dataset. The centroids are depicted in Fig. 7a at their PC1, PC2-coordinates with the numbered markers.

Cluster label	PC1	PC2	PC3	PC4	PC5
MMIJ-1	-0.33	-0.05	-0.04	-0.02	0.01
MMIJ-2	0	0.17	-0.08	0.05	0.02
MMIJ-3	0.38	0.38	-0.01	0.05	0
MMIJ-4	0.35	-0.02	0.04	-0.09	-0.06
MMIJ-5	0	-0.22	-0.16	0.07	-0.04
MMIJ-6	0.74	-0.4	0.02	0	0.12
MMIJ-7	0.14	-0.33	0.44	0.09	0.03
MMIJ-8	-0.36	0.36	0.45	0.04	0.02

To investigate the characteristics of each cluster, Fig. 10a–c show how the clusters are distributed over the years, months, and hours of the day. The upper panel shows that the inter-annual variability is limited, which asserts that the results can safely be generalised to the lifetime of a wind energy system ($\sim$20 years). In contrast to the other panels, the absolute frequency is on the y-axis and serves to show which part of the total dataset is represented by each of the clusters. Fig. 10d–f show the relative
5 frequency of each cluster for different conditions in terms of wind speed, wind direction, and atmospheric stability. As for the logarithmic profile fits, the stability for each sample is classified using Table 1.

Here, we derive the stability class distributions using the bulk Richardson number, $\mathrm{Ri_B}$, converted to the Obukhov length, L, using Eqs. 5 and 6. The data from either ERA5 or DOWA could be used to derive $\mathrm{Ri_B}$, however, we found that using the data from the two lowest ERA5 model levels, i.e., $\sim$10–31 m yields the most realistic values. We use the arithmetic mean of
10 the model level heights for z in order to convert $\mathrm{Ri_B}$ to L.
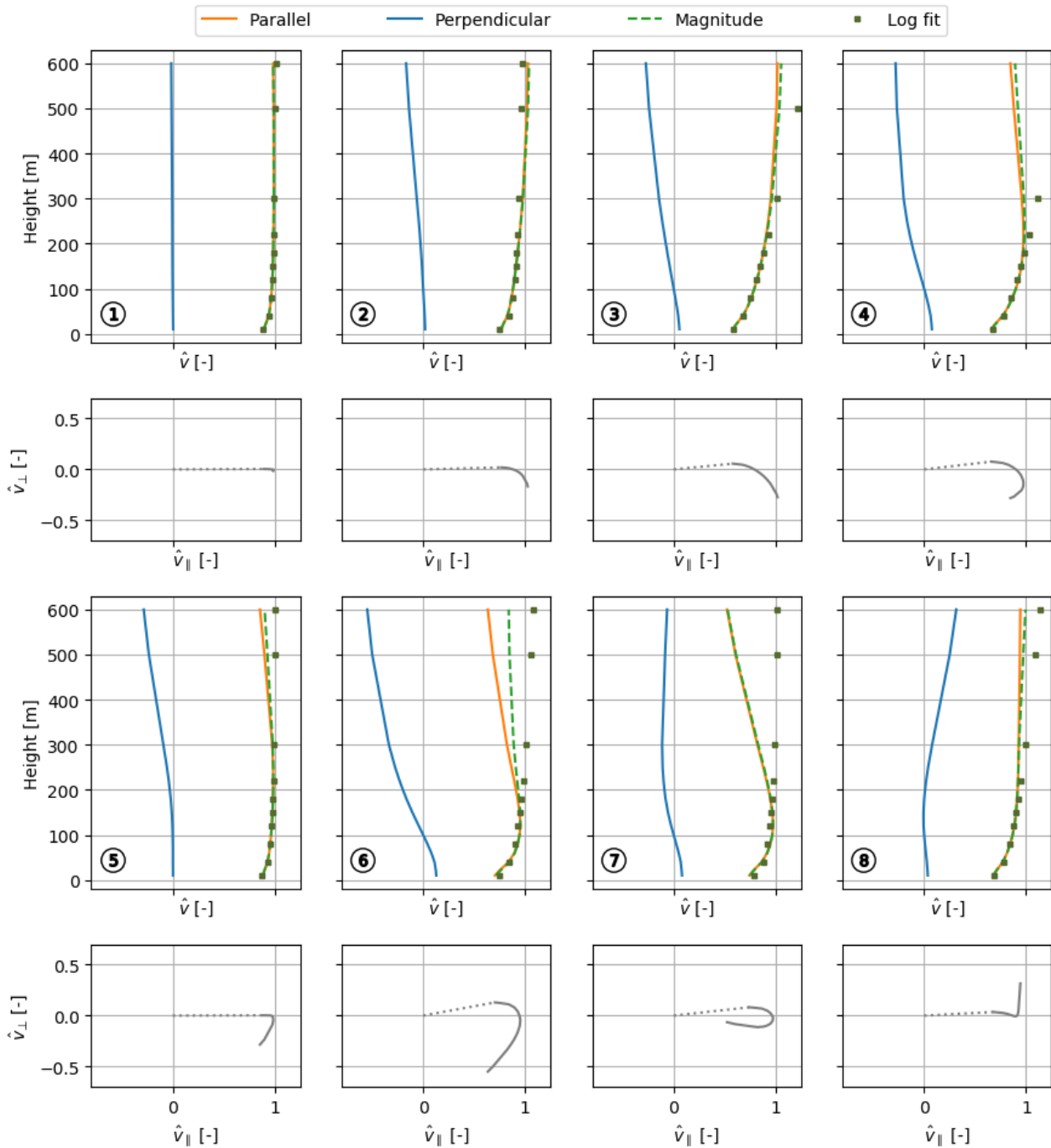
Figure 8. The eight cluster-mean wind profile shapes of the offshore clusters (MMIJ-1–8). Each shape is depicted by the normalised wind speed components with height (first and third rows) with the corresponding hodograph below (second and fourth rows). Logarithmic profile fits are plotted alongside the shapes. In the hodographs, the lowest points are connected to the origins with dotted lines and the highest points are the loose ends. All plots share the same x-axis.
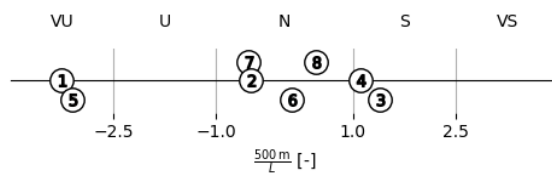
Figure 9. Obukhov lengths (plotted as $500\,\mathrm{m}/L$) found by fitting logarithmic profiles to the offshore cluster-mean wind profile shapes in Fig. 8. The stability classes are adopted from Table 1.
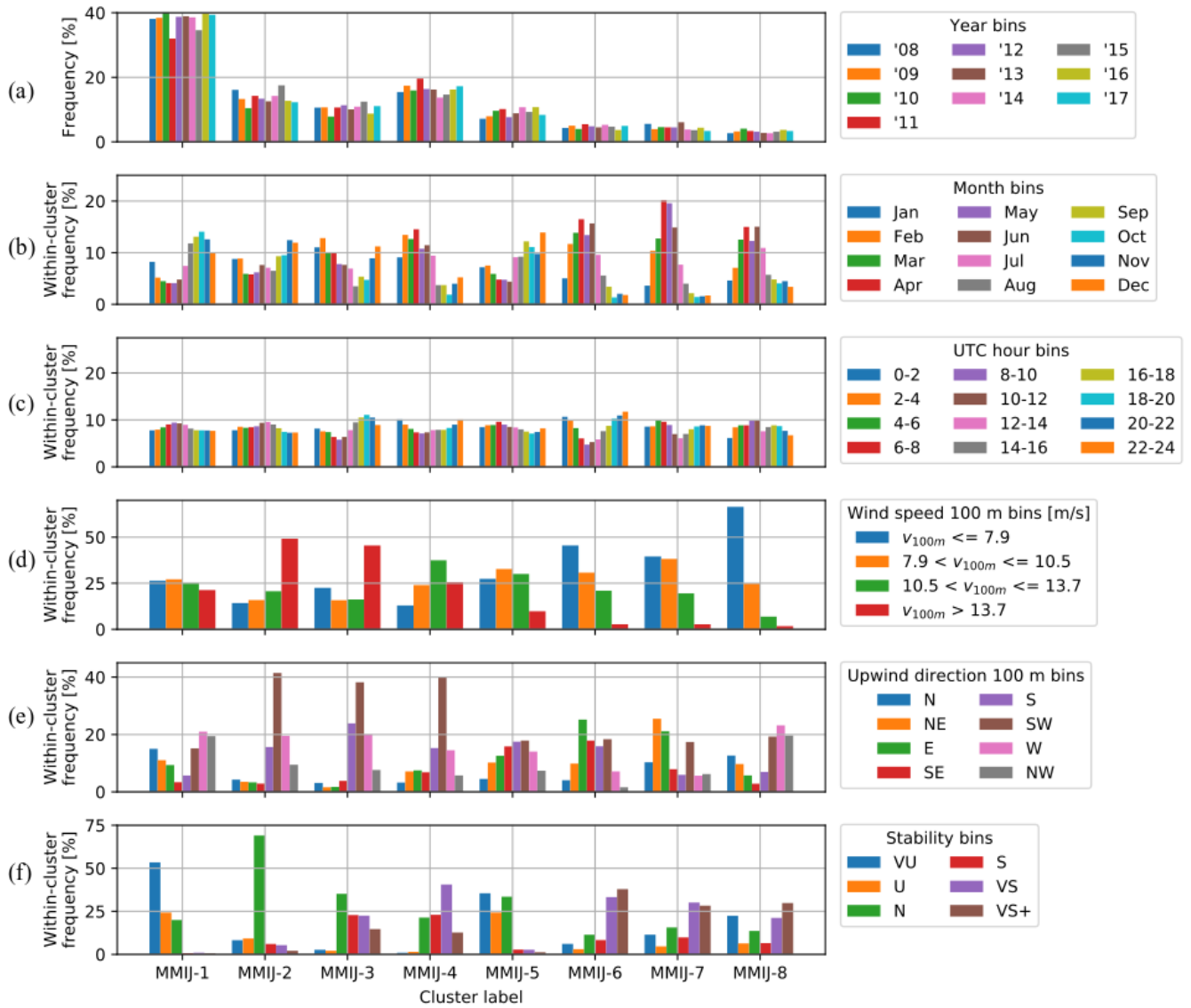
Figure 10. Frequency distributions broken down into bins by time of occurrence, reference wind speed and direction, and atmospheric stability for the filtered offshore dataset. The wind speed bin limits are chosen such that the frequency over all clusters for each bin is roughly the same. The stability bins correspond to the classes in Table 1 together with the VS+ bin ($Ri_B \geq 0.2$). The other distributions have equal bin widths.

4.2 Interpretation of the offshore cluster representation

By examining Figs. 8 and 9, we can see how the cluster-mean wind profile shapes differ from standard logarithmic profiles, particularly above the surface layer. Moreover, by referring to Fig. 10, it is possible to investigate the conditions under which each of the clusters occur, and to gain insight into their physical origins.

Figure 8 shows that the MMIJ-1 and 2 profile shapes are described well with logarithmic profiles. The MMIJ-1 profile shape suggests a well-mixed convective (unstable) profile with little wind shear or veer. MMIJ-1 occurs predominantly in autumn and is slightly more frequent in the morning hours. The wind is more frequently weak or moderate than strong and mostly coming from the westerly, north-westerly or northerly directions. Furthermore, this cluster occurs predominantly during (very) unstable conditions. These observations make sense as in autumn, the relatively warm sea water favours neutral to unstable stratification; the dominant wind directions have long fetches over sea which allows the boundary layer to develop an equilibrium profile.

The MMIJ-2 and 3 profile shapes display increased levels of shear compared to that of MMIJ-1. The MMIJ-2 profile shape closely resembles a neutral logarithmic profile up to 600 m, whereas that of MMIJ-3 only shows a good fit with a stable logarithmic profile in the surface layer. These clusters occur typically during strong winds, predominantly from the south-west. Strong south-westerly winds are characteristic of the wind climate at this mid-latitude location, which is dominated by the frequent passage of low-pressure systems. The relatively strong winds explain why we see the highest occurrence of near-neutral conditions, especially for MMIJ-2. For MMIJ-3, we also see frequent (very) stable conditions. Simultaneously, we observe that MMIJ-2 occurs more often in the late autumn and MMIJ-3 in winter and the start of the spring. The colder sea water in spring favours the formation of stable stratification, which explains the difference in stability distribution between the two clusters. Stable stratification suppresses turbulent mixing, which helps to sustain a strong wind shear, consistent with the increasing wind shear and veer seen in Figs. 7a and 8.

The MMIJ-4–7 profile shapes are all (slightly) jet-like with relatively large deviations from logarithmic profiles at greater altitudes. The wind direction and stability distributions associated with the MMIJ-4 cluster are correlated with south-westerly winds and stable stratification. The seasonal cycle is very pronounced and peaks in spring, when stable stratification is frequent. The winds recorded for MMIJ-4 are mostly moderate to strong. The distributions associated with the MMIJ-5 cluster are very similar to those of MMIJ-1, with the exception of the wind direction distribution, which shows an opposite trend. The frequent winds with a southerly component typically have shorter fetches over sea than the north and westerly winds seen for MMIJ-1. The hodograph of the MMIJ-5 profile shape indicates a rather abrupt kink around 140 m, suggesting a discontinuity such as an (internal) boundary-layer top. The MMIJ-6 profile shape shows a maximum at 120 m. Although the magnitude profiles of MMIJ-5 and 6 look somewhat similar, the MMIJ-6 profile shape veers more and gradually. The MMIJ-7 profile shape shows the most pronounced jet-like shape, also peaking around 120 m. MMIJ-6 and 7 occur almost exclusively for very stable conditions in spring and for weak wind situations. Both clusters occur predominantly for (north)easterly winds and show a diurnal cycle with fewer occurrences around noon. Such a diurnal cycle is in agreement with various studies that have linked low-level jets and the diurnal variation of both the land-sea temperature difference and the intensity of turbulent mixing (e.g., Burk and Thompson, 1996; Parish, 2000; Mahrt et al., 2014; Shapiro et al., 2016).

The hodographs of MMIJ-5 and 8 both show an abrupt kink around 140 m. However, the wind direction turns anticlockwise with height above the kink for MMIJ-8, which is opposite to the veering of the other profile shapes. Despite the peculiarities of the wind direction profiles, the magnitude profiles of MMIJ-5 and 8 are described reasonably well with very unstable and neutral logarithmic profiles, respectively. MMIJ-8 occurs mostly in spring, under stable conditions, and more often for winds with a westerly rather than a southerly component. Note that this shape belongs to an incohesive cluster and, therefore, gives a relatively poor representation of the cluster samples.

4.3 Comparing the on- and offshore cluster representations

The clustering is repeated using the dataset for the onshore location of the met mast Cabauw. The eight resulting clusters are referred to as MMC-1–8. The results of the PC analysis of the onshore dataset are shown in Fig. 11 and compared to those of the offshore dataset, shown in Fig. 2. A logarithmic profile with roughness length z_0=0.1 m, a representative value for the area surrounding the mast (Verkaik, 2006), is fitted to the mean wind profile shape as before. With a stability function value corresponding to L=476 m, the mean profile shape shows a good fit with a stable logarithmic profile below 200 m. Above that, the fitted logarithmic profile rapidly diverges from the mean shape. A higher wind shear is observed than for the offshore location due to the higher surface roughness. The hodograph in the lower left panel shows that also the wind veer is substantially increased. Despite the apparent differences in mean shape, the PC1 and PC2 profiles are very similar for both reference locations. The average PC profiles of the two locations are plotted alongside the onshore PC profiles using the dashed lines. The coordinate system of Figs. 4a and b represent the average PC profiles. Both figures share the same coordinate system, which enables a direct comparison between the reference locations.

The distribution in Fig. 4b shows a similar pattern to Fig. 4a: a dense, confined group of samples, marked with the left ellipse, with a tail of samples extending from this group at around 45 degrees towards the right ellipse. In general, the samples of the onshore dataset are more spread out than the offshore samples, particularly along the PC1 axis. Also the confined group is less dense for the onshore location. Figure 7 shows that, for both locations, the samples of these confined groups belong to the on- and offshore clusters with number 1. The remaining onshore clusters with monotonic wind speed and veering profiles, MMC-2–4, account for most of the tail, see Fig. 12. Note that the cluster algorithm produces arbitrary labels for each class. We have manually renumbered them such that the numbering is more or less aligned between onshore and offshore clusters. This allows us to draw parallels between them and show that the resulting profiles are very similar between both locations, e.g., the first offshore clusters (MMIJ-1–3) also have monotonic profiles.

Again, logarithmic profiles with roughness length z_0=0.1 m are fitted to the cluster-mean wind profile shapes, and plotted alongside them in Fig. 12. The values found for the Obukhov lengths and the corresponding stability classes are presented in Fig. 13. The profile shapes for MMC-1 to MMC-3 show an increase in wind shear. Between MMIJ-3 and MMIJ-4, we see an increased wind veer, though reduced wind shear. The profile shapes for MMC-5–7 are (slightly) jet-like, as is the case for the offshore clusters MMIJ-4–7. MMC-5 and MMC-6 have similar wind velocity magnitude profiles with a relatively weak wind speed maximum around 200 m, but MMC-6 shows a much stronger wind veer. MMC-7 shows the strongest fall-off above 200 m. Like its offshore counterpart, MMC-8 is characterised by anticlockwise turning and an abrupt kink in the wind profile,

which is most clearly visible in the hodograph view. Recall that the offshore wind profile shape for MMIJ-5 also showed a kink, albeit, in combination with clockwise turning. We do not see these features for any of the MMC profile shapes.

Figure 14 shows that MMC-3 is the most frequent cluster in the (filtered) onshore dataset, with a frequency of 20.6 %. Where for the offshore location one distinct dominant cluster is identified, the frequency distribution over the first five onshore clusters

5   is more balanced. As for the offshore clusters MMIJ-6–8, the onshore clusters MMC-6–8 are less frequent.

Figure 14 shows clusters that typically occur during spring/summer (MMC-1, MMC-7 and MMC-8) or autumn/winter (MMC-2–6). The diurnal cycles of the onshore location are highly pronounced in contrast to those for the offshore location. This effect is caused by the lower heat capacity of the land surface which promotes a more immediate heat transfer to or from the atmosphere. In the presence of daytime solar irradiation, convection is created, and well-mixed profiles are expected,

10   whereas at night, stable stratification is more frequent. MMC-1 and MMC-2 predominantly occur during the day and MMC-3–8 during the night. Note that low-level jets, and stable conditions in general, occur almost exclusively at night. The patterns in the times of occurrences indicate a pronounced diurnal cycle in atmospheric stability for the onshore location, whereas for the offshore location the seasonal cycle is more pronounced. Figs. 10d and 14d have almost identical bin distributions, but different bin widths, and thus different wind speed distributions. Note that the wind speed bin limits are chosen such that the

15   frequency over all clusters for each bin is roughly the same, yielding different bin widths for the two reference locations. Also the wind direction and stability distributions show similar patterns for both locations. Only the stability distribution of MMC-5 and MMIJ-5 differ substantially.

In conclusion, we see that very similar cluster-mean wind profile shapes have been identified for the on- and offshore reference locations. Moreover, similar profiles seem to be related to similar conditions in terms of wind speed, wind direction,

20   and atmospheric stability. The strongest winds typically act to neutralise the stratification, leading to monotonic profiles with relatively little veer. These profiles are relatively well captured by logarithmic wind profiles. For weaker winds, atmospheric stability acts to enhance wind shear and veer, up to the point where low-level jets start to be observed. However, whereas stability at the offshore location is governed by a clear seasonal cycle in the underlying sea surface, stability over land is regulated by the relatively rapid diurnal heating cycle of the land surface. Over sea, the wind direction also seems to play a

25   more pronounced role, since it controls the characteristics of the prevailing fetch.
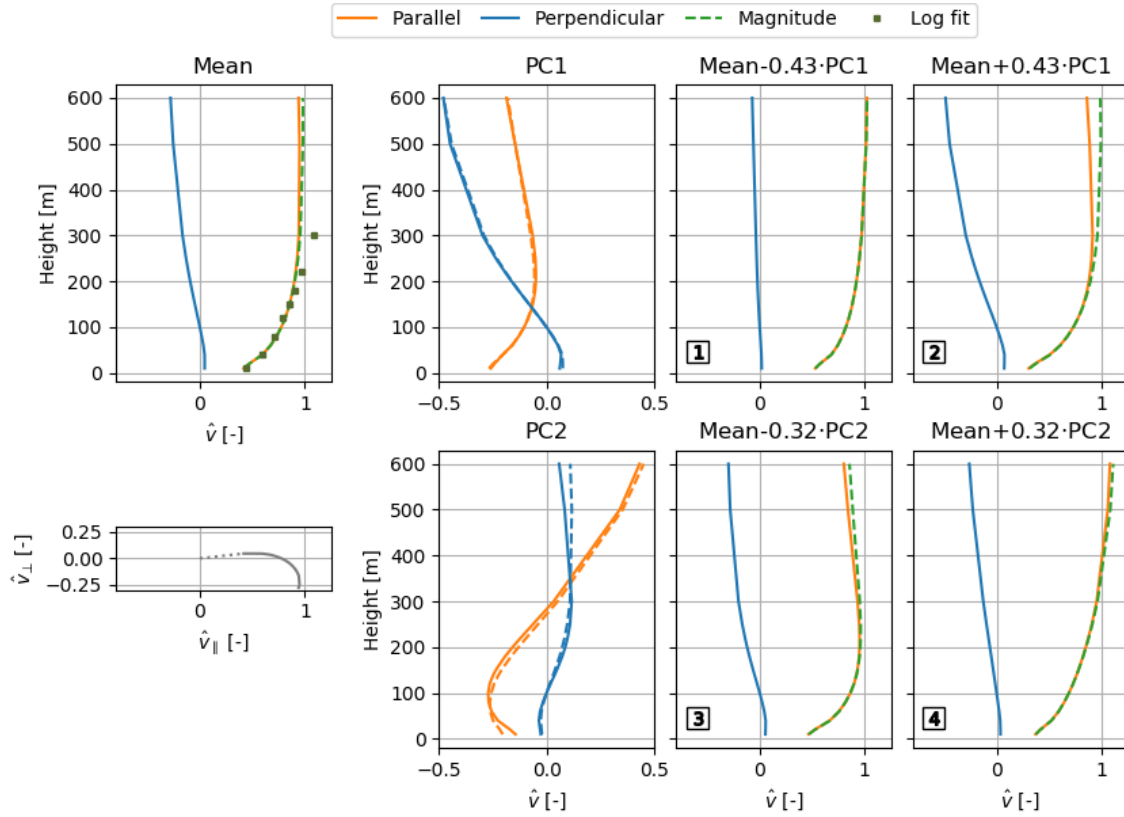
Figure 11. Mean wind profile shape and corresponding logarithmic profile fit (top-left) and corresponding hodograph (bottom-left), composition of the first and second PCs (second column), and PC multiplicands superimposed on the mean wind profile shape (using minus and plus one standard deviation as multipliers for the third and fourth columns, respectively) for the filtered onshore dataset. The wind profile shape numbers 1–4 refer to the markers in Fig. 4b. The average PC profiles of the two reference locations are plotted alongside the onshore PCs using the dashed lines (second column).
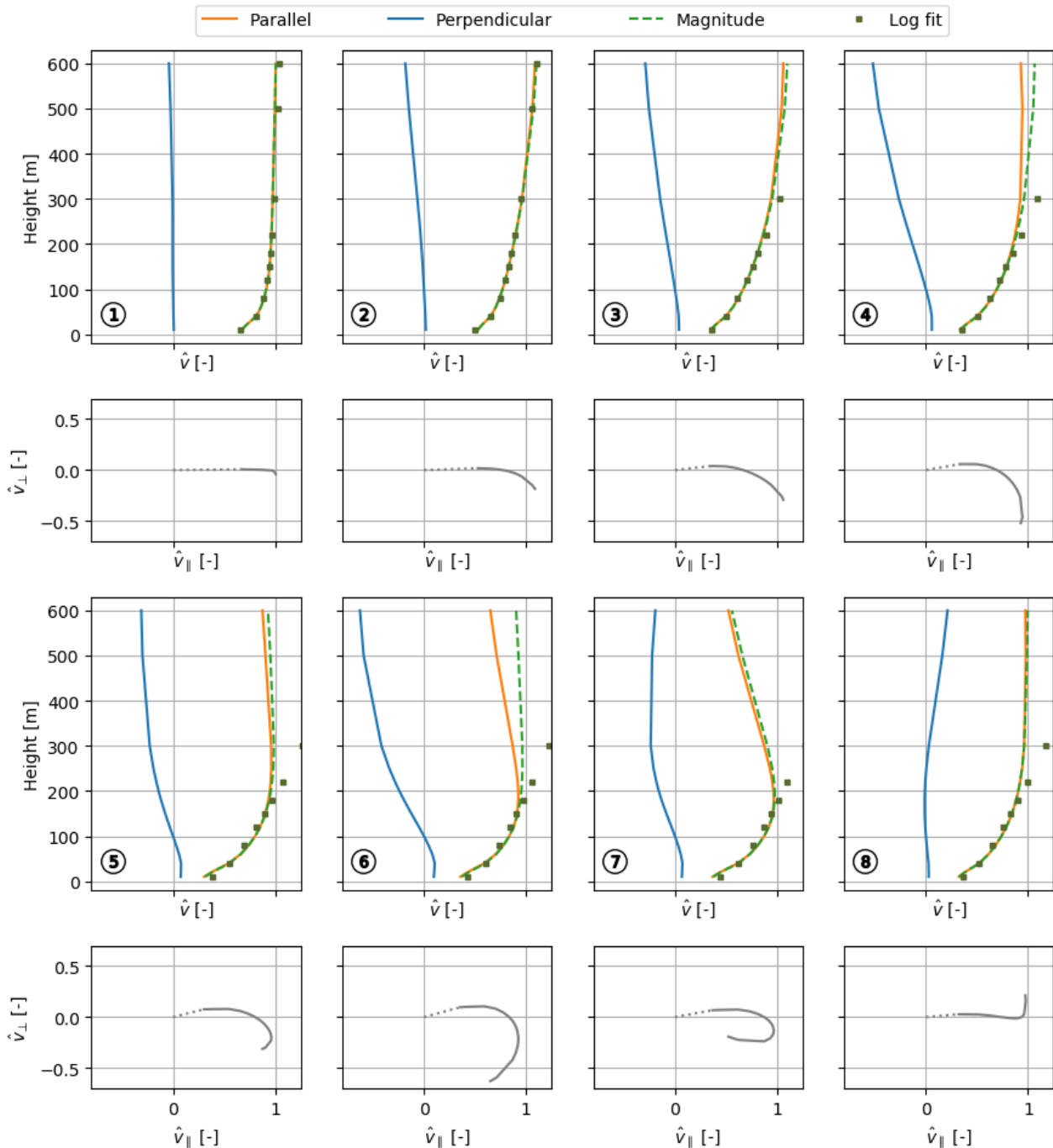
Figure 12. The eight cluster-mean wind profile shapes of the onshore clusters (MMC-1–8). Each shape is depicted by the normalised wind speed components with height (first and third rows) with the corresponding hodograph below (second and fourth rows). Logarithmic profile fits are plotted alongside the shapes. In the hodographs, the lowest points are connected to the origins with dotted lines and the highest points are the loose ends. All plots share the same x-axis.
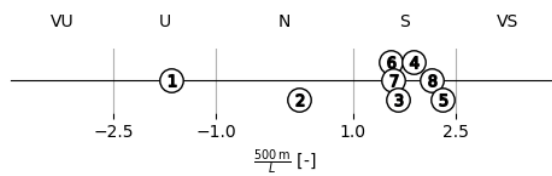
Figure 13. Obukhov lengths (plotted as $500\,\mathrm{m}/L$) found by fitting logarithmic profiles to the onshore cluster-mean wind profile shapes in Fig. 12. The stability classes are adopted from Table 1.
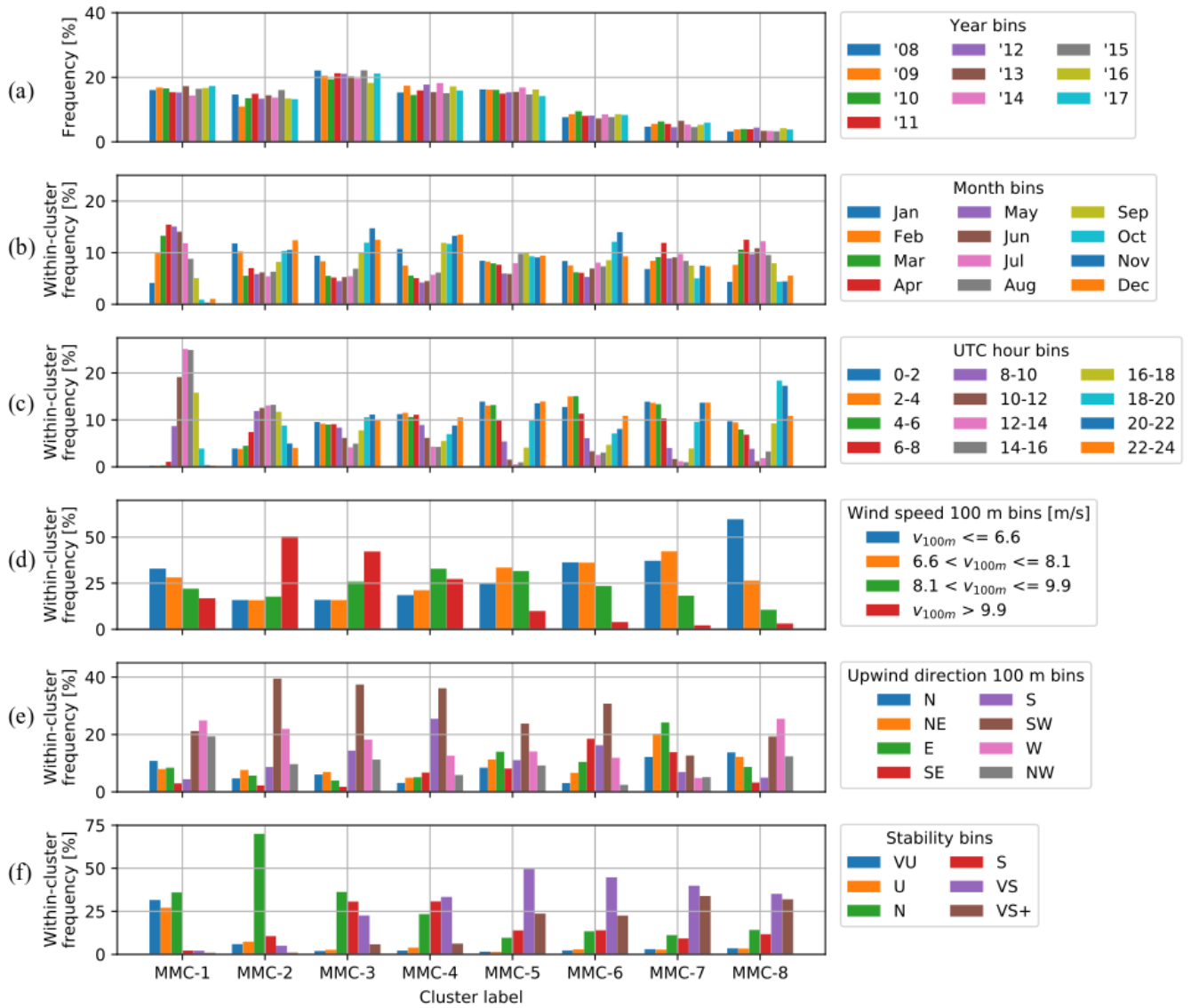
Figure 14. Frequency distributions broken down into bins for time of occurrence, reference wind speed and direction, and atmospheric stability for the filtered onshore dataset. The wind speed bin limits are chosen such that the frequency over all clusters for each bin is roughly the same. The stability bins correspond to the classes in Table 1 together with the VS+ bin ($\text{Ri}_B \geq 0.2$). The other distributions have equal bin widths.

4.4 Spatial frequency distribution of wind profile shape clusters

So far, we have shown that similar clusters and, consequently, similar wind profile shapes are identified for both onshore and offshore locations. Here, we apply our clustering algorithm on a dataset that includes wind data for a variety of locations. The multi-location dataset (filtered to exclude low wind samples) includes wind data from 45 DOWA grid points that are selected

5   such that onshore, coastal, and offshore locations are equally represented. For each location type, 15 grid points are chosen (pseudo-randomly) to yield a good coverage of the full DOWA domain (50778 grid points in total). The sampled grid points are marked on the map in Fig. 1. Our aim is to give some insight into the spatial variability of wind profile characteristics, in particular to see how the clustering approach highlights profile characteristics of the on- and offshore environments. In principle, the multi-location approach gives a set of profile shapes that could be used for an AEP assessment, though a site specific set would

10   be better suited if a more accurate assessment is required. So, whilst we increase the applicability of the cluster representation to a larger area by keeping the number of clusters the same, we compromise on the accuracy. As mentioned before, increasing the number of clusters is inherent to reducing the error. The number of clusters can be increased until a suitable accuracy is attained. Here, we still use eight clusters, as it suffices to give an impression of the spatial variability of the wind profile shapes. The eight resulting multi-location clusters are referred to as ML-1–8.

15   Figure 15 shows the cluster-mean wind profile shapes for each of the multi-location clusters. Each sample of every grid point in the DOWA domain is assigned to the cluster with the closest centroid. For each cluster, a map is generated showing the spatial distribution of its frequency of occurrence, see Fig. 16. Note that the colour scale is different for each map so that spatial patterns are easier to observe. It is interesting to compare the multi-location clusters with the site-specific clusters identified earlier. With a frequency of 48.5 %, ML-1 is dominant at the met mast IJmuiden. Therefore, we expect it to be similar to

20   MMIJ-1, the dominant cluster resulting from the offshore analysis. Comparing Figs. 8 and 15 indeed shows that the cluster-mean wind profile shapes of ML-1 and MMIJ-1 look alike. Similarly, ML-7 has the highest frequency at the met mast Cabauw, i.e. 21.7 %, and has a profile shape somewhere in between those of MMC-3 and 4, the most frequent clusters resulting from the onshore analysis. Every multi-location cluster is manually linked to the single location clusters based on resemblance of their cluster-mean wind profile shapes, see Table 3.

25   The maps in Fig. 16 show a distinct division between clusters that mostly occur over sea (ML-1–3) and over land (ML-4–8). The latter group is sub-divided into coastal and onshore clusters, see Table 3. The sharply defined patterns in the frequency maps of ML-5–8 coincide with terrain features and thus suggest a strong relationship between the clusters and terrain. Other site characteristics such as recurring weather systems and land cover also affect the clusters and thus the frequency maps. Over land the frequency maps of ML-5 and ML-6 suggest an inverse relationship: the frequency of ML-5 peaks at high

30   elevations, whereas that of ML-6 is highest in the river valley in the lower right corner of the DOWA domain. A similar inverse relationship is observed between ML-7 and ML-8. Also, the frequency maps of ML-7 and ML-8 show contours coinciding with the elevation map, though the relationship between the frequency and elevation is not as direct as for ML-5 and ML-6.

Table 3. Classification of the multiple-location clusters and frequencies of occurrence of the clusters at the on- and offshore reference locations (met masts Cabauw and IJmuiden).

Cluster label	Class	Similar single location cluster(s)	Frequency at offshore location	Frequency at onshore location
ML-1	offshore	MMIJ-1	48.5 %	5.8 %
ML-2	offshore	MMIJ-2, 3	22.0 %	4.2 %
ML-3	offshore	MMIJ-4, 6	14.1 %	4.2 %
ML-4	coastal	MMC-1	8.6 %	16.1 %
ML-5	onshore/coastal	MMC-2	3.0 %	17.4 %
ML-6	onshore	MMC-6	2.0 %	13.3 %
ML-7	onshore	MMC-3, 4	1.2 %	21.7 %
ML-8	onshore	MMC-5	0.6 %	17.3 %
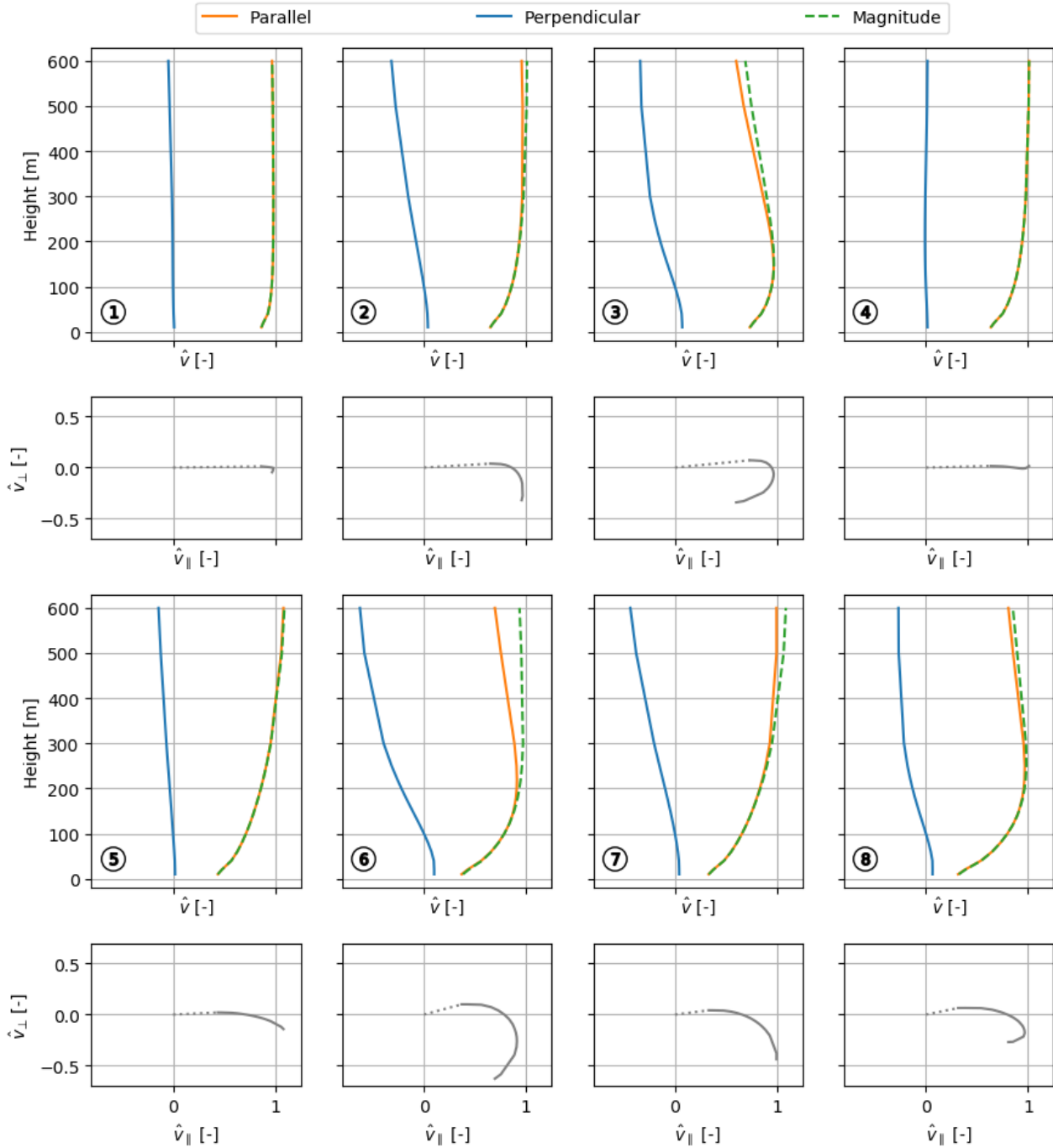
Figure 15. The eight cluster-mean wind profile shapes of the multi-location clusters (ML-1–8). Each shape is depicted by the normalised wind speed components with height (first and third rows) with the corresponding hodograph below (second and fourth rows). In the hodographs, the lowest points are connected to the origins with dotted lines and the highest points are the loose ends. All plots share the same x-axis.
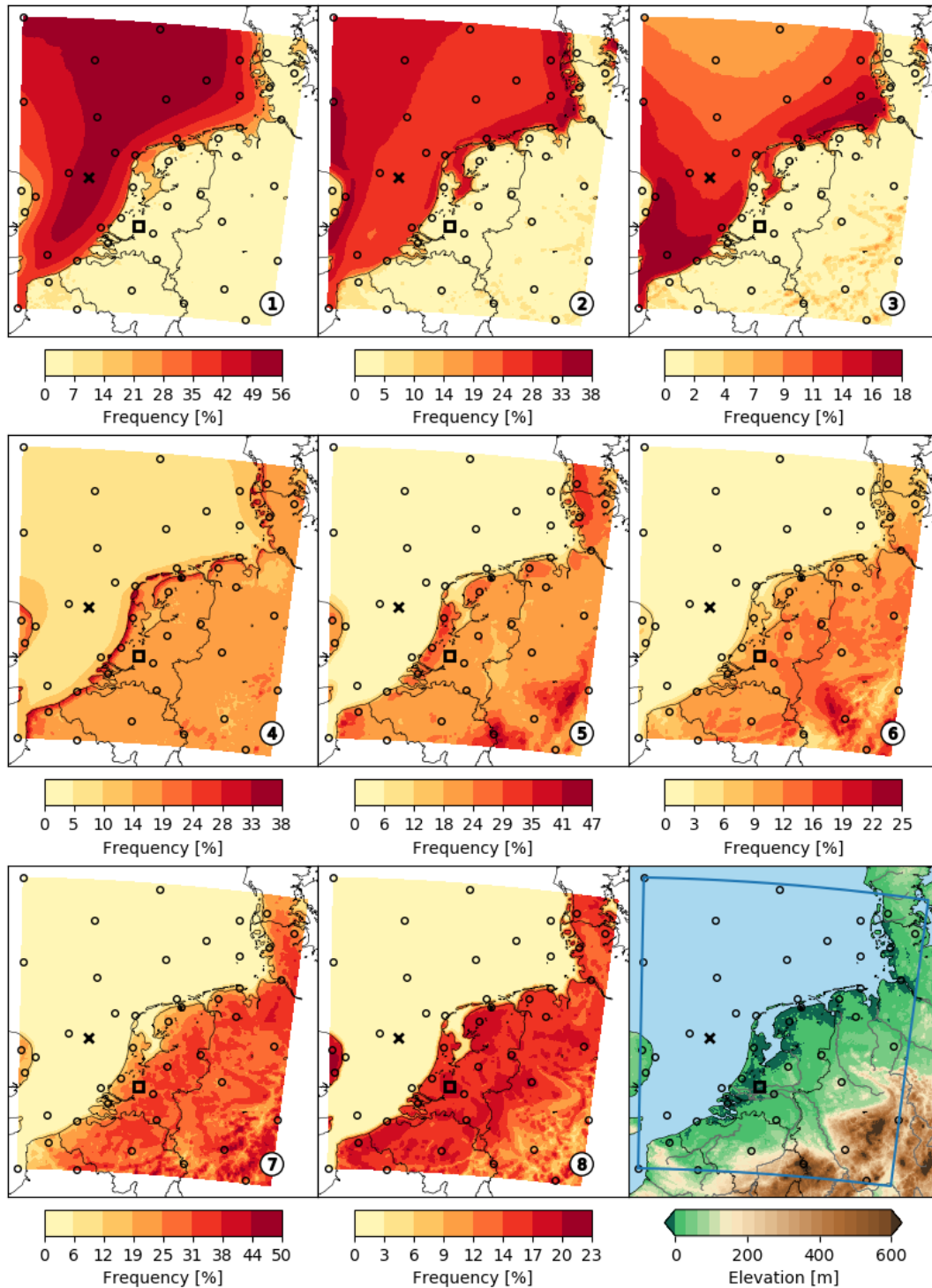
Figure 16. Frequency of occurrence of each multiple-location cluster (ML-1–8) mapped over the DOWA domain. The × and □ markers depict the reference locations of the met masts IJmuiden and Cabauw. The ○ markers show the sampled grid points. The lower right plot is a repetition of Fig. 1.

5 Efficient AWE production estimation using the cluster representation

With AWE technology maturing and approaching the deployment stage, the community is debating how to uniformly define the performance of AWE systems (Van Hussen et al., 2018). A generally applicable set of wind profile shapes is considered to be an important step to facilitate the standardisation of wind conditions for which AWE systems are rated in terms of power production. In this section, we demonstrate how the wind resource representations obtained using the clustering procedure can be used for estimating the AEP of a pumping AWE system. An advantage of AWE systems over tower-based wind turbines is that they have access to winds higher up. This advantage is limited when low-shear wind profiles are frequent at the installation site, as is the case offshore, but unusual for onshore locations. Deploying an AWE system at an onshore location thus requires a more variable operational approach. For this reason, we demonstrate the AEP estimation for the met mast Cabauw location using the eight clusters from the single location analysis (Sect. 4.3). A separate power curve is generated for each cluster using its cluster-mean wind profile shape. The power curves together with the corresponding wind speed distributions yield the AEP contributions of the clusters. Finally, the sensitivity of the total AEP to the number of clusters is evaluated.

5.1 Constructing the power curves

A pumping AWE system is alternating between reeling the tether in and out and thereby consuming and producing power, respectively. The relatively high lift force generated by the kite during reel-out and long reel-out phase yields a positive net energy output. The specific operational approach differs between AWE concepts and may require different performance models for calculating the generated power. We evaluate a flexible-kite system using the quasi-steady model (QSM) developed by Van der Vlugt et al. (2019) specifically for this concept. The cluster representation can in principle be used together with any performance model for estimating the AEP.

Flexible-kite systems typically sweep a large height range during the pumping cycle, which requires pronounced transitions between these two working phases (Salma et al., 2019). Figure 17 shows the distinct phases of a pumping flexible-kite system. During the reel-out phase, the kite flies figure-of-eight manoeuvres in a fast cross-wind motion. After the reel-out phase, the kite stops flying cross-wind, de-powers, and flies towards zenith. Once reeled back in, the kite steers down, flies towards the starting position of the reel-out phase, and starts a next cycle. The QSM idealises and represents the pumping cycle using three phases: the reel-in, transition, and reel-out phase. The transition between the reel-out and reel-in phases is not modelled separately, but is included in the reel-in phase. The model does not resolve the cross-wind flight manoeuvres during the reel-out phase but represents them by an average cross-wind flight state with constant values for the elevation, azimuth, and course angle. The motion of the kite is approximated by moving it along the idealised flight path according to the computed steady-state kite speed.

The QSM assumes a steady wind field with a constant wind direction and only a vertical variation in the wind speed. Therefore, we consider only the magnitude profiles of the cluster-mean wind profile shapes in the calculations. The unidirectional wind profile approximation is equivalent to hypothetically knowing the wind direction profile and steering the kite to correct for direction changes. We use the system properties of the 20 kW technology demonstrator of Delft University of Technology
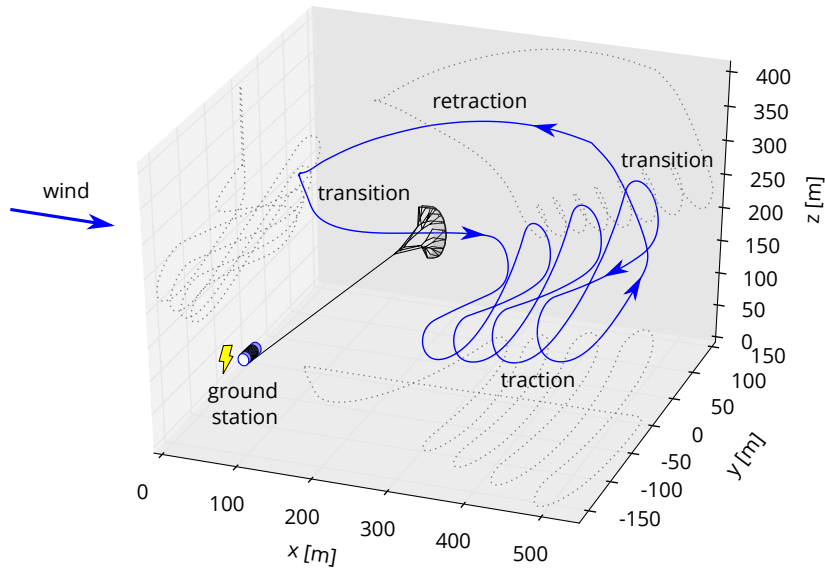
Figure 17. Flight path of the flexible-kite, pumping AWE system (kite & drum not to scale) adapted from Fechner (2016).

given in Table 4. The QSM uses constant values for the lift and drag coefficients of the powered and de-powered kite. In reality, the coefficients vary and representative values of the leading edge inflatable V3 kite are selected based on the experiment of Oehler and Schmehl (2019).

Table 4. Constant system properties that are required as model input for the QSM. C_L and C_D stand for lift and drag coefficients, respectively. The kite and tether properties follow from the work of Oehler and Schmehl (2019). The other properties are chosen by judgment of the authors.

Kite properties		Tether properties		Operational limits		Representative reel-out state	
Projected area	$19.75\,\mathrm{m}^2$	Density	$724\,\mathrm{kg\,m}^{-3}$	Min. reeling speed	$2\,\mathrm{m\,s}^{-1}$	Azimuth angle	$13°$
Mass	$22.8\,\mathrm{kg}$	Diameter	$4\,\mathrm{mm}$	Max. reeling speed	$10\,\mathrm{m\,s}^{-1}$	Course angle	$100°$
$C_{L,\mathrm{powered}}$	0.9	$C_{D,\mathrm{tether}}$	1.1	Min. tether force	$300\,\mathrm{N}$		
$C_{D,\mathrm{powered}}$	0.2			Max. tether force	$5000\,\mathrm{N}$		
$C_{L,\mathrm{depowered}}$	0.2						
$C_{D,\mathrm{depowered}}$	0.1						

Calculating the energy production of an AWE system requires characterising the (maximum) mean cycle power for a large variety of wind conditions. The mean cycle power depends on the operational settings that control the cycle trajectory and phase durations. These cycle settings include the forces applied to the tether during reel-in and reel-out. The values of the cycle settings are chosen such that they yield maximum mean cycle power. The reel-in tether force should allow a fast retraction of the kite, while limiting the energy consumption. During the transition phase, the reeling speed is kept zero unless tether force

limits are exceeded. During reel-out, the tether force should yield a high energy production, while letting the reel-out phase comprise most of the cycle duration. For high wind speeds, the system runs into its maximum tether force and reeling speed limits. Increasing the elevation angle of the reel-out path generally indirectly de-powers the kite and alleviates the tether force. Controlling the elevation angle can thereby expand the wind speed range that allows safe operations. Although not considered here, the kite could also be de-powered directly by controlling $C_{L,\mathrm{powered}}$. The effective pumping length of the trajectory is the difference between the minimum and maximum tether length during reel-out and is included as a cycle setting. The minimum tether length is fixed at $200\,\mathrm{m}$.

We use numerical optimisation to determine the cycle settings that maximises the mean cycle power. Table 5 lists the optimisation variables and their respective limits. Imposing a lower bound on the tether force ensures that the kite stays tensioned, as required for a flexible-kite. The upper bound corresponds to the maximum allowed tether force. The remaining limits are chosen by judgment of the authors. The optimisation uses the sequential quadratic programming algorithm (SLSQP) that is part of pyOpt (Perez et al., 2012). This class of algorithms is generally seen as a good general-purpose method for differentiable constrained non-linear problems. The power curves required for the AEP estimation relate the mean cycle power to the scaling parameter used for de-normalising the cluster-mean wind profile shapes of MMC-1–8. Given the profile shape, this scaling parameter can be prescribed as a wind speed at any height. We use the wind speed at $100\,\mathrm{m}$. By stepping through a range of wind speeds between cut-in and cut-out, a power curve is constructed for each of the clusters. At each step, the profile shape is scaled using the respective wind speed to yield the absolute wind profile. An optimisation is then performed using this wind profile as input.

Table 5. Optimisation variables used for maximising the mean cycle power and corresponding limits defining the parameter space. The limits are chosen by judgment of the authors.

Parameter	Lower bound	Upper bound
Reel-out force	300 N	5000 N
Reel-in force	300 N	5000 N
Reel-out elevation angle	25°	60°
Pumping length tether	150 m	250 m

Prior to performing the optimisations, we determine the cut-in and cut-out wind speeds at $100\,\mathrm{m}$ for each wind profile shape. The cut-in limit is assumed to be the smallest wind speed for which, along the whole reel-out path, feasible steady flight states are found with the QSM. The cut-out limit is determined by the criterion that the pumping cycle should complete at least one figure-of-eight manoeuvre (at an elevation angle of 60 degrees). This criterion becomes more critical at high wind speeds, as the reel-out phase gets shorter. The QSM as presented by Van der Vlugt et al. (2019) does not resolve the cross-wind flight motion. However, this motion can also be approximated as a transition through steady flight states, yielding an approximate duration of the figure-of-eight manoeuvre. Dividing the total duration of the reel-out phase by the average duration of a figure-of-eight manoeuvre yields the number of cross-wind manoeuvres flown.

Scaling each wind profile shape such that the wind speed at 100 m equals the previously determined cut-in and cut-out wind speeds yields the respective absolute wind profiles, shown in Fig. 18. The cut-in profiles have the same wind speed at roughly 80 m, which is the kite height at the start of the reel-out phase for the minimum elevation angle employed at low winds. This indicates that, for every wind profile, the cut-in criterion is critical at the start of the reel-out phase rather than at the end.

5   The cut-out profiles exhibit roughly the same wind speed at 300 m, which is the kite height at the end of the reel-out phase for the maximum elevation angle and tether length employed at high winds. The cut-out wind conditions for an AWE system are ambiguous when defined by wind speeds at a certain height without defining the profile shape. However, since the cut-out profiles all intersect at roughly 300 m, characterising the cut-out wind speed at this height yields a reasonably precise definition for all profile shapes. Similarly, the cut-in wind speed is well defined at 80 m. At 100 m, MMC-3 and MMC-7 show the lowest

10 and highest cut-out wind speed, respectively.
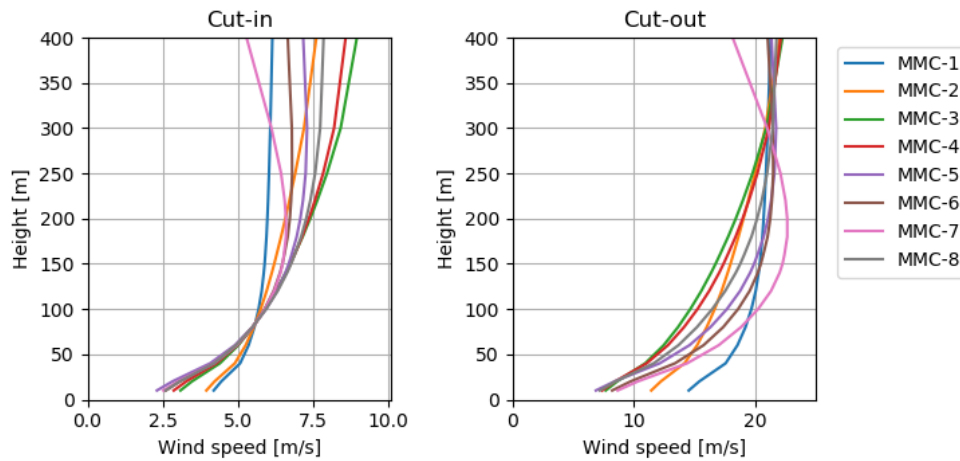
Figure 18. The cut-in (left) and cut-out (right) wind profiles that follow from scaling the profile shapes from Fig. 12 such that the wind speed at 100 m equals the cut-in and cut-out wind speeds, respectively.

Figure 19 shows the idealised cycle trajectories that follow from the optimisations for the cluster-mean wind profile shape of MMC-1. The wind speeds for which the trajectories are depicted highlight changes in the operational approach. The optimal pumping tether length coincides with its upper bound for all wind speeds. The reel-out elevation angle of the flight trajectory for v_{100m}=10.5 m s^{-1} coincides with its lower bound. For higher wind speeds, an increased inclination of the reel-out path yields

15 a higher mean cycle power. At roughly v_{100m}=16 m s^{-1}, the maximum mean cycle power is reached with the kite completing only one cross-wind pattern. Above 16 m s^{-1} wind speed, the criterion of completing one cross-wind pattern is driving the elevation angle to higher values until reaching its upper bound for v_{100m}=19.7 m s^{-1}, above which no feasible solution exists.

The calculated power curves are shown in Fig. 20. Note that plotting the mean cycle power against the wind speed at 300 m would yield curves that end at roughly the same wind speed. Up to roughly v_{100m}=8.5 m s^{-1}, all the power curves are similar.

20 Above this wind speed, the curves flatten off and become different from one another. The MMC-3 and MMC-7 curves show
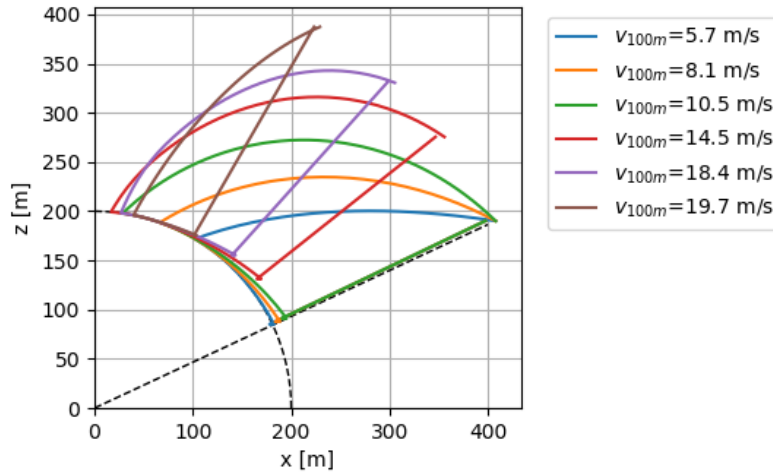
Figure 19. The optimal idealised cycle trajectories for six wind profiles with the same profile shape, i.e., that of cluster MMC-1, but different scaling. The wind speeds for which the trajectories are depicted highlight changes in the operational approach. The angle of inclination of the straight dotted line is the minimum elevation angle. The radius of the dotted quarter circle shows the fixed minimum tether length.

the lowest and highest maximum mean cycle power, respectively. In conclusion, a pronounced low-level jet is favoured over a high-shear wind profile shape in terms of the power production of an AWE system.
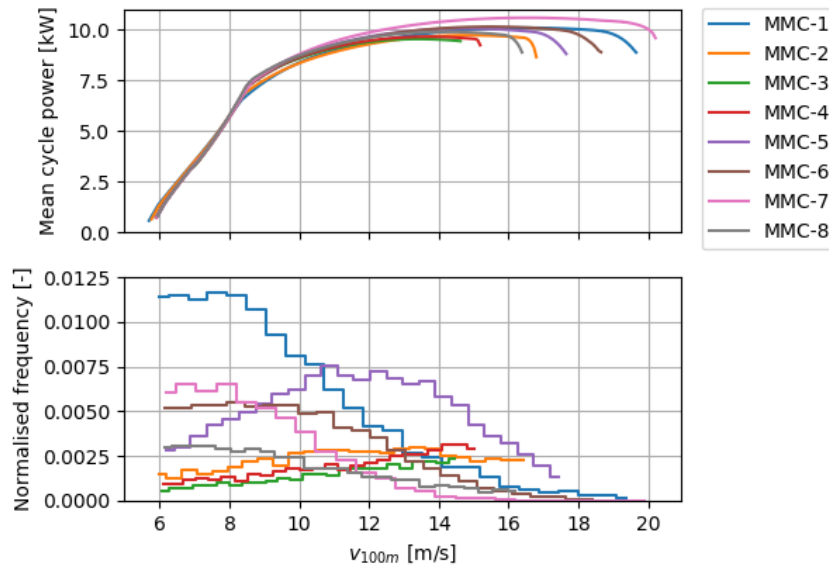
Figure 20. Power curves obtained by performance optimisations using the cluster-mean wind profile shapes of MMC-1–8 (top). Wind speed distribution of the samples within each cluster using the full onshore dataset (bottom). Only the frequencies between cut-in and cut-out are depicted and, for illustrative purposes, every four wind speed bins are aggregated and shown as a single bin.

5.2 Estimating the annual energy production

The previously constructed power curves are used for calculating the average generated power of the AWE system:

$$\bar{P} = \sum_{i=1}^{n_c} \int_0^\infty p_i(v_{\text{norm}}) \cdot P_i(v_{100\text{m}}) \, \mathrm{d}v_{\text{norm}} \approx \sum_{i=1}^{n_c} \sum_{j=1}^{n_b} \frac{f_{i,j}}{n_s} \cdot P_i(v_{100\text{m}}) \quad , \tag{9}$$

in which p_i is the wind speed probability for cluster i, P_i is the power curve for the wind profile shape of cluster i, v_{norm} is the normalisation wind speed, $v_{100\text{m}}$ the wind speed at $100\,\text{m}$ height, n_c is the number of clusters, n_b is the number of wind speed bins and n_s is the total number of samples. The integral in the expression is solved numerically using 100 wind speed bins between the cut-in and cut-out wind speeds at $100\,\text{m}$. In the resulting right hand side expression, p_i is approximated by normalising the sample frequency $f_{i,j}$ for cluster i and wind speed bin j in the onshore dataset. A large number of bins is used to mitigate numerical errors. The probability of each cluster is characterised using the normalisation wind speed of the pre-processing. The equivalent speed at $100\,\text{m}$ height is calculated to determine the frequency in the wind speed bin, using: $v_{100\text{m}} = v_{\text{norm}} \cdot \hat{v}_{i,100\text{m}}$, in which $\hat{v}_{i,100\text{m}}$ is the normalised wind speed of the wind profile shape of cluster i at $100\,\text{m}$ height. The resulting wind speed distributions are shown in the lower panel of Fig. 20. Multiplying the average generated power by the hours in a year gives the AEP estimate.

The AEP at the onshore location is evaluated for the MMC and ML cluster representations from Sects. 4.3 and 4.4, respectively. Moreover, the number of clusters used for the representations is varied to assess how many clusters are needed for the AEP to converge to a steady value, see Fig. 21. The trend for the MMC representation converges to around $36\,\text{MWh}$ for a large number of clusters. For four or more clusters, the AEP error is within three percent of the converged value and for 14 or more clusters, there is virtually no more variation in the AEP and the steady solution is reached. The error can be mostly explained by the inaccuracy of the cluster wind resource representation, but also by the numerically obtained power curves and inaccuracies in the numerical integration. The AEP trend for the MMC representation converges faster than that for the ML representation, since the former is generated specifically for the evaluated location. The MMC and ML trends show a similar difference to the converged value at 16 and 32 clusters, respectively, suggesting that the ML representation needs twice the number clusters to yield the same accuracy as the MMC representation. Note that assumptions in the performance model also affect the convergence, e.g., neglecting the change of wind direction with height is expected to increase the convergence rate. How many clusters to use depends on the application of the AEP calculation. In a preliminary design optimisation, where the computational cost is critical, four MMC-clusters may be a sensible choice. For more detailed design studies, 14 MMC-clusters would be more suitable.

More than 50 optimisations are used to obtain each power curve, yielding highly detailed curves. With only a small compromise on the level of detail, half of the number of optimisations can be used, which thus halves the computational cost. Assuming that a four-cluster representation provides sufficient accuracy and 25 optimisations are used for generating a single power curve, 100 performance optimisations are required for the AEP calculation. In case of a brute force calculation, in which for every hour a separate optimisation is performed, 8760 optimisations are required per year. When only evaluating a single

year, the number of optimisation required by the presented methodology is already two orders of magnitude less. Also, it does not require more optimisations when evaluating a longer period, however, the computational effort for the clustering increases.
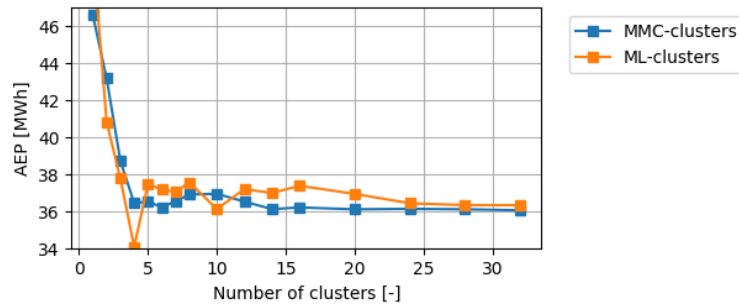
Figure 21. AEP convergence for the onshore reference location using the MMC and ML wind resource representations.

6 Conclusions

We have presented a data-driven methodology to identify a set of wind profile shapes using clustering that can be used to
5   characterise the wind resource for AWE systems. These shapes go beyond the height range for which conventional wind profile relationships, such as the logarithmic profile, are developed. Moreover, they allow the quantification of phenomena such as the occurrence of non-monotonic wind profile shapes such as low-level jets. The Dutch Offshore Wind Atlas is used for demonstrating the methodology for an on- and offshore reference location.

    Prior to a principal component analysis, the DOWA wind profiles are expressed in terms of the wind velocity at the $100\,\mathrm{m}$
10   reference height and normalised. The PC analysis shows that three PCs already account for about $90\,\%$ of the variance. The first and second PCs are very similar for the datasets of the onshore and offshore locations. The first PC characterises mostly wind veer, whereas the second PC characterises mostly wind shear. Moreover, the analysis reveals a natural structure of the data in the principal component space with two relatively dense groups of data points. The data points for the onshore location are more spread out, indicating a larger variety of wind profile shapes.

15   The dataset is partitioned using k-means clustering and the cluster-mean wind profile shapes are determined. In the cluster wind resource representation, each sample's vertical wind variation is approximated using these shapes, thereby, the wide variety of wind conditions in the DOWA dataset is reduced to a reasonable number of wind profile shapes. Although some variability remains in the profile shapes of the samples assigned to each cluster, the cluster-mean shapes nonetheless allow a better representation of the vertical wind variation than relying on a monotonic logarithmic profile. Indeed, the accuracy of the
20   representation using three or more clusters is already higher than that of the representation using logarithmic wind profiles up to $600\,\mathrm{m}$. The cluster-mean wind profile shapes of the offshore eight-cluster representation shows three monotonic profiles, four jet-like profiles, and an anticlockwise-turning, kinked profile. Very similar cluster-mean wind profile shapes have been identified for the onshore location occurring under similar conditions. A single set of clusters is generated that is representative

for the whole DOWA domain and used to analyse the spatial variability of the frequency of occurrence of the clusters. The cluster frequency maps indicate a clear distinction between onshore and offshore clusters. The sharply defined patterns in the frequency maps of the onshore clusters coincide with terrain features and thus suggest a strong relationship between the clusters and terrain.

5   The AEP of a flexible-kite, pumping AWE system is estimated using the onshore cluster representation. For each cluster-mean wind profile shape, a power curve is obtained by using the quasi-steady model in power production optimisations. The highest power is found for the shape with a pronounced low-level jet. Together with the respective wind speed distributions, the power curves yield the AEP contributions of the clusters. The relationship between the estimated AEP and the number of site specific clusters shows that the AEP error is within three percent of the converged value when using four or more clusters.

10 For 14 or more clusters, there is virtually no more variation in the AEP estimation. For a four-cluster representation and using 25 optimisations for constructing the power curve of a single cluster, 100 optimisations are required for the AEP estimation against 8760 for an hourly brute-force calculation. The proposed methodology is thereby roughly two orders of magnitude faster.

The methodology presented has the capability to produce a single set of wind profile shapes that is valid for a large area.

15 Such a set can facilitate the standardisation of wind conditions for which AWE systems are rated in terms of power production. Moreover, the multi-location cluster representation enable an assessment of which installation site is best for an AWE system in terms of its AEP, which makes this methodology a very powerful tool for project developers. In future work, the role of the performance model in making the AEP calculation is further investigated.

Author contributions.   Analysis and preparation of the paper were performed by MS, under the supervision of RS and SJW. PCK provided
20 input on meteorology and data analysis and contributed to writing the result section.

Competing interests.   The authors declare that they have no conflict of interest.

Acknowledgements.   Without the publicly available Dutch Offshore Wind Atlas by the KNMI and the ERA5 dataset by the ECMWF, this work would not have been possible. Mark Schelbergen and Roland Schmehl have received financial support by the project REACH (H2020-FTIPilot-691173), funded by the European Union's Horizon 2020 research and innovation programme under grant agreement No. 691173,
25 and AWESCO (H2020-ITN-642682) funded by the European Union's Horizon 2020 research and innovation programme under the Marie Skłodowska-Curie grant agreement No. 642682.

References

Amante, C. and Eakins, B. W.: ETOPO1 1 Arc-Minute Global Relief Model: Procedures, Data Sources and Analysis. NOAA Technical Memorandum NESDIS NGDC-24. National Geophysical Data Center, NOAA, https://doi.org/10.7289/V5C8276M, 2009.

Basu, S.: A simple recipe for estimating atmospheric stability solely based on surface-layer wind speed profile, Wind Energy, 21, 937–941, https://doi.org/10.1002/we.2203, 2018.

Bechtle, P., Schelbergen, M., Schmehl, R., Zillmann, U., and Watson, S.: Airborne wind energy resource analysis, Renew. Energ., 141, 1103 – 1116, https://doi.org/https://doi.org/10.1016/j.renene.2019.03.118, 2019.

Bengtsson, L., Andrae, U., Aspelien, T., Batrak, Y., Calvo, J., de Rooy, W., Gleeson, E., Hansen-Sass, B., Homleid, M., Hortal, M., Ivarsson, K.-I., Lenderink, G., Niemelä, S., Nielsen, K. P., Onvlee, J., Rontu, L., Samuelsson, P., Muñoz, D. S., Subias, A., Tijm, S., Toll, V., Yang, X., and Køltzow, M. Ø.: The HARMONIE–AROME Model Configuration in the ALADIN–HIRLAM NWP System, Mon. Weather Rev., 145, 1919–1935, https://doi.org/10.1175/MWR-D-16-0417.1, 2017.

Brown, A. R., Beljaars, A. C. M., Hersbach, H., Hollingsworth, A., Miller, M., and Vasiljevic, D.: Wind turning across the marine atmospheric boundary layer, Q. J. Roy. Meteor. Soc., 131, 1233–1250, https://doi.org/10.1256/qj.04.163, 2005.

Burk, S. D. and Thompson, W. T.: The Summertime Low-Level Jet and Marine Boundary Layer Structure along the California Coast, Mon. Weather Rev., 124, 668–686, https://doi.org/10.1175/1520-0493(1996)124<0668:TSLLJA>2.0.CO;2, 1996.

Copernicus Climate Change Service: ERA5: Fifth generation of ECMWF atmospheric reanalyses of the global climate. Copernicus Climate Change Service Climate Data Store (CDS), https://cds.climate.copernicus.eu/cdsapp#!/home, 2017.

Duran, P., Basu, S., Meissner, C., and Adaramola, M.: Automated classification of simulated wind field patterns from multi-physics ensemble forecasts, Wind Energy, https://doi.org/10.1002/we.2462, 2019.

Fechner, U.: A Methodology for the Design of Kite-Power Control Systems, Ph.D. thesis, Delft University of Technology, https://doi.org/10.4233/uuid:85efaf4c-9dce-4111-bc91-7171b9da4b77, 2016.

Floors, R., Peña, A., and Gryning, S.-E.: The effect of baroclinicity on the wind in the planetary boundary layer, Q. J. Roy. Meteor. Soc., 141, 619–630, https://doi.org/10.1002/qj.2386, 2015.

Gryning, S.-E., Batchvarova, E., Brümmer, B., Jørgensen, H., and Larsen, S.: On the extension of the wind profile over homogeneous terrain beyond the surface boundary layer, Bound.-Lay. Meteorol., 124, 251–268, https://doi.org/10.1007/s10546-007-9166-9, 2007.

Heilmann, J. and Houle, C.: Economics of Pumping Kite Generators, in: Airborne Wind Energy, edited by Ahrens, U., Diehl, M., and Schmehl, R., pp. 271–284, Springer, Berlin Heidelberg, https://doi.org/10.1007/978-3-642-39965-7_15, 2013.

Holtslag, M., Bierbooms, W., and van Bussel, G.: Extending the diabatic surface layer wind shear profile for offshore wind energy, Renew. Energ., 101, 96 – 110, https://doi.org/https://doi.org/10.1016/j.renene.2016.08.031, 2017.

Holtslag, M. C., Bierbooms, W. A. A. M., and van Bussel, G. J. W.: Estimating atmospheric stability from observations and correcting wind shear models accordingly, J. Phys. Conf. Ser., 555, 012 052, https://doi.org/10.1088/1742-6596/555/1/012052, 2014.

Kalverla, P. C.: Characterisation of offshore winds for energy applications, Ph.D. thesis, Wageningen University, https://edepot.wur.nl/498797, 2019.

Kalverla, P. C., Steeneveld, G.-J., Ronda, R. J., and Holtslag, A. A.: An observational climatology of anomalous wind events at offshore meteomast IJmuiden (North Sea), J. Wind Eng. Ind. Aerod., 165, 86 – 99, https://doi.org/https://doi.org/10.1016/j.jweia.2017.03.008, 2017.

Kalverla, P. C., Duncan Jr., J. B., Steeneveld, G.-J., and Holtslag, A. A. M.: Low-level jets over the North Sea based on ERA5 and observations: together they do better, Wind Energ. Sci., 4, 193–209, https://doi.org/10.5194/wes-4-193-2019, 2019.

Kelly, M. and Gryning, S.-E.: Long-Term Mean Wind Profiles Based on Similarity Theory, Bound.-Lay. Meteorol., 136, 377–490, https://doi.org/10.1007/s10546-010-9509-9, 2010.

5 Mahrt, L., Vickers, D., and Andreas, E. L.: Low-Level Wind Maxima and Structure of the Stably Stratified Boundary Layer in the Coastal Zone, J. Appl. Meteorol. Clim., 53, 363–376, https://doi.org/10.1175/JAMC-D-13-0170.1, 2014.

Malz, E., Koenemann, J., Sieberling, S., and Gros, S.: A reference model for airborne wind energy systems for optimization and control, Renew. Energ., 140, 1004 – 1011, https://doi.org/https://doi.org/10.1016/j.renene.2019.03.111, 2019.

Malz, E., Hedenus, F., Göransson, L., Verendel, V., and Gros, S.: Drag-mode airborne wind energy vs. wind turbines: An analysis of power

10 production, variability and geography, Energy, 193, 116 765, https://doi.org/https://doi.org/10.1016/j.energy.2019.116765, 2020a.

Malz, E., Verendel, V., and Gros, S.: Computing the power profiles for an airborne wind energy system based on large-scale wind data [Submitted], Renew. Energ., 2020b.

Monin, A. and Obukhov, A.: Basic laws of turbulent mixing in the ground layer of the atmosphere (in Russian), Trudy Geofiz. Inst. Akad. Nauk SSSR, 151, 163–187, 1954.

15 Oehler, J. and Schmehl, R.: Aerodynamic characterization of a soft kite by in situ flow measurement, Wind Energ. Sci., 4, 1–21, https://doi.org/10.5194/wes-4-1-2019, 2019.

Optis, M., Monahan, A., and Bosveld, F. C.: Moving Beyond Monin–Obukhov Similarity Theory in Modelling Wind-Speed Profiles in the Lower Atmospheric Boundary Layer under Stable Stratification, Bound.-Lay. Meteorol., 153, 497–514, https://doi.org/10.1007/s10546-014-9953-z, 2014.

20 Parish, T. R.: Forcing of the Summertime Low-Level Jet along the California Coast, J. Appl. Meteorol., 39, 2421–2433, https://doi.org/10.1175/1520-0450(2000)039<2421:FOTSLL>2.0.CO;2, 2000.

Park, J., Basu, S., and Manuel, L.: Large-eddy simulation of stable boundary layer turbulence and estimation of associated wind turbine loads, Wind Energy, 17, 359–384, https://doi.org/10.1002/we.1580, 2014.

Pedregosa, F., Varoquaux, G., Gramfort, A., Michel, V., Thirion, B., Grisel, O., Blondel, M., Prettenhofer, P., Weiss, R., Dubourg, V.,

25 Vanderplas, J., Passos, A., Cournapeau, D., Brucher, M., Perrot, M., and Duchesnay, E.: Scikit-learn: Machine Learning in Python, J. Mach. Learn. Res., 12, 2825–2830, 2011.

Perez, R. E., Jansen, P. W., and Martins, J. R. R. A.: pyOpt: A Python-Based Object-Oriented Framework for Nonlinear Constrained Optimization, Struct. Multidiscip. O., 45, 101–118, https://doi.org/10.1007/s00158-011-0666-3, 2012.

Peterson, E. W. and Hennessey, J. P.: On the Use of Power Laws for Estimates of Wind Power Potential, J. Appl. Meteorol., 17, 390–394,

30 https://doi.org/10.1175/1520-0450(1978)017<0390:OTUOPL>2.0.CO;2, 1978.

Ranjha, R., Svensson, G., Tjernström, M., and Semedo, A.: Global distribution and seasonal variability of coastal low-level jets derived from ERA-Interim reanalysis, Tellus A, 65, 20 412, https://doi.org/10.3402/tellusa.v65i0.20412, 2013.

Ranneberg, M., Wölfle, D., Bormann, A., Rohde, P., Breipohl, F., and Bastigkeit, I.: Fast Power Curve and Yield Estimation of Pumping Airborne Wind Energy Systems, in: Airborne Wind Energy: Advances in Technology Development and Research, edited by Schmehl, R.,

35 pp. 623–641, Springer, Singapore, https://doi.org/10.1007/978-981-10-1947-0_25, 2018.

Salma, V., Ruiterkamp, R., Kruijff, M., Paassen, M. M. R. v., and Schmehl, R.: Current and Expected Airspace Regulations for Airborne Wind Energy Systems, in: Airborne Wind Energy – Advances in Technology Development and Research, edited by Schmehl, R., Green Energy and Technology, chap. 29, pp. 703–725, Springer, Singapore, https://doi.org/10.1007/978-981-10-1947-0_29, 2018.

Salma, V., Friedl, F., and Schmehl, R.: Reliability and Safety of Airborne Wind Energy Systems, Wind Energy, 23, 340–356, https://doi.org/10.1002/we.2433, 2019.

Shapiro, A., Fedorovich, E., and Rahimi, S.: A Unified Theory for the Great Plains Nocturnal Low-Level Jet, J. Atmos. Sci., 73, 3037–3057, https://doi.org/10.1175/JAS-D-15-0307.1, 2016.

5   Sommerfeld, M., Crawford, C., Monahan, A., and Bastigkeit, I.: LiDAR-based characterization of mid-altitude wind conditions for airborne wind energy systems, Wind Energy, 22, 1101–1120, https://doi.org/10.1002/we.2343, 2019.

Van der Vlugt, R., Bley, A., Noom, M., and Schmehl, R.: Quasi-Steady Model of a Pumping Kite Power System, Renew. Energ., 131, 83–99, https://doi.org/10.1016/j.renene.2018.07.023, 2019.

Van Hussen, K., Dietrich, E., Smeltink, J., Berentsen, K., van der Sleen, M., Haffner, R., and Fagiano, L.: Study on challenges in the
10   commercialisation of airborne wind energy systems, Tech. Rep. ECORYS Report PP-05081-2016, European Commission, Brussels, https://doi.org/10.2777/87591, 2018.

Verkaik, J. W.: On Wind and Roughness over Land, Ph.D. thesis, Wageningen University, 2006.

Watson, S., Moro, A., Reis, V., Baniotopoulos, C., Barth, S., Bartoli, G., Bauer, F., Boelman, E., Bosse, D., Cherubini, A., Croce, A., Fagiano, L., Fontana, M., Gambier, A., Gkoumas, K., Golightly, C., Latour, M. I., Jamieson, P., Kaldellis, J., Macdonald, A., Murphy,
15   J., Muskulus, M., Petrini, F., Pigolotti, L., Rasmussen, F., Schild, P., Schmehl, R., Stavridou, N., Tande, J., Taylor, N., Telsnig, T., and Wiser, R.: Future emerging technologies in the wind power sector: A European perspective, Renew. Sust. Energ. Rev., 113, 109 270, https://doi.org/10.1016/j.rser.2019.109270, 2019.

Wijnant, I. L., van den Brink, H. W., and Stepek, A.: North Sea wind climatology part 1: a review of existing wind atlases, Tech. rep., KNMI, 2015.

20   Wijnant, I. L., van Ulft, B., van Stratum, B., Barkmeijer, J., Onvlee, J., de Valk, C., Knoop, S., Kok, S., Marseille, G. J., Klein Baltink, H., and Stepek, A.: The Dutch Offshore Wind Atlas (DOWA): description of the dataset, Tech. rep., KNMI, 2019.